MOX-Report No. 86/2021

A Mesoscale Computational Model for Microvascular Oxygen Transfer

Possenti, L.; Cicchetti, A.; Rosati, R.; Cerroni, D.; Costantino, M.L.; Rancati, T.; Zunino, P.

MOX, Dipartimento di Matematica
Politecnico di Milano, Via Bonardi 9 - 20133 Milano (Italy)

mox-dmat@polimi.it http://mox.polimi.it

A mesoscale computational model for microvascular oxygen transfer

Luca Possenti[1,2,*], Alessandro Cicchetti[2,*], Riccardo Rosati[1], Daniele Cerroni[3], Maria Laura Costantino[1], Tiziana Rancati[2], and Paolo Zunino[3]

[1]Department of Chemistry, Materials and Chemical Engineering "Giulio Natta", Politecnico di Milano
[2]Prostate Cancer Program, Fondazione IRCCS Istituto Nazionale dei Tumori di Milan
[3]MOX, Department of Mathematics, Politecnico di Milano
[*]Authors contributed equally

December 14, 2021

Abstract

We address a mathematical model for oxygen transfer in the microcirculation. The model includes blood flow and hematocrit transport coupled with the interstitial flow, oxygen transport in the blood and the tissue, including capillary-tissue exchange effects. Moreover, the model is suited to handle arbitrarily complex vascular geometries. The purpose of this study is the validation of the model with respect to classical solutions and the further demonstration of its adequacy to describe the heterogeneity of oxygenation in the tissue microenvironment. Finally, we discuss the importance of these effects in the treatment of cancer using radiotherapy.
Keywords: oxygen transfer, microcirculation, mesoscale model.

1 Introduction

The microcirculation serves vital oxygen and nutrient supply in tissues and controls functions in living systems. For this reason, microcirculation has been thoroughly studied in vitro and in vivo in the fundamental sciences [23, 68]. Recently, analyses by means of mathematical models and numerical simulations have contributed significantly to revealing the physiological function and interaction between blood flow and the surrounding tissues that are difficult to observe otherwise, see [41, 47, 17] just to make a few examples. Modeling and computational approaches of microcirculation have recently become a vivid

area of research. Starting from a few seminal contributions [45, 16, 59, 15], yet addressing realistic portions of tissue, to very recent achievements where whole organ simulations are at reach [32, 65].

These achievements were made possible by a suitable blending of mathematical modeling and computational methods. However, the microcirculation involves phenomena at very different spatial and temporal scales. A naive modeling approach based on the brute force application of computational fluid dynamics tools would fail to consider the complex interaction between the microcirculation and the tissue. Conversely, the most successful attempts to model microcirculation are characterized by embedding into one characteristic spatial scale the relevant effects that are active at scales larger and smaller than the main one. In synthesis, such approaches are effectively called a *mesoscale* description of microcirculation [60].

The purpose of this work is to develop a model for microcirculation and oxygen transfer that is particularly suited to describe the phenomena at the level of the tissue microenvironment (sub-millimeter scale), where heterogeneities of the distribution of oxygen in the tissue due to the possibly irregular layout of the micro-vessels are well documented [68]. As will be discussed later on, such effects are particularly important in pathologies such as cancer.

We aim at describing these effects with good physical accuracy from a mechanistic standpoint. For this reason, we include the following effects in our model, among the main factors addressed in the extensive review [45]: blood flow with variable viscosity and hematocrit transport coupled with fluid extravasation and interstitial flow; oxygen transport in blood, described using continuum models for dissolved and hemoglobin-bound oxygen; oxygen transport in tissue, based on advection, diffusion and reaction effects; the coupling of the oxygen transport models in blood and tissue by capillary-tissue exchange effects, described in the case of non-equilibrium thermodynamics and for arbitrarily complex geometries.

The mesoscale approach previously addressed is the ideal framework for the interaction of all these effects in a reasonably complex vascular network. Indeed, the modeling framework that we adopt stems from the seminal work on the method of Green's functions applied to microcirculation [59]. However, we depart from such an approach because the phenomena addressed before are formulated in the continuum setting in our model. A model reduction technique is then applied to the equations defined in the vasculature, transforming the network of vessels into a one-dimensional (1D) graph. Its coupling with the three-dimensional (3D) surrounding environment is addressed by the mathematically sound coupling operators described and analyzed in [31]. The main advantage of this approach consists in its modularity: the vascular and tissue regions can be discretized independently and the numerical solution of the former is greatly simplified by the dimensionality reduction.

Concerning these challenging objectives, the purpose of this work is twofold. On the one hand, we aim at validating the proposed model with respect to well known and accepted oxygen transfer models that are valid in simplified conditions, such as the Krogh's model. On the other hand, we discuss the mathematical and computational platform's ability to describe realistic clini-

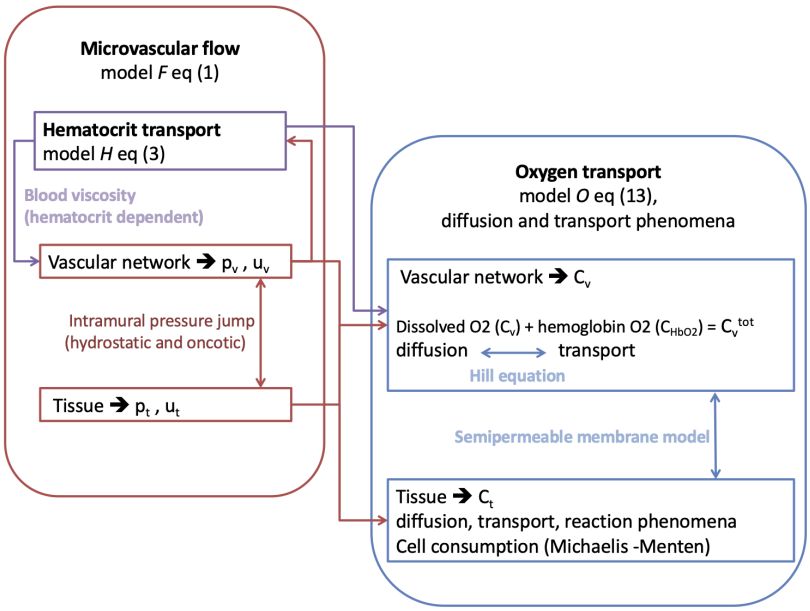

Figure 1: The general layout of the model illustrating its components, the phenomena described by the governing equations and their interactions.

cal scenarios relevant for cancer treatment, specifically, radiotherapy. Indeed, even though this treatment is based on the damage of the cell genetic material, preclinical and clinical studies have highlighted the so-called *oxygen effect* that impacts tumor sensitivity to ionizing radiation. The linear-quadratic model, the most popular radiobiological model for describing tumor cell death, has been ameliorated to include the differences in cell survival due to oxygen concentration in the tissue. Here, we will discuss how the oxygen transfer model can be used study the biological factors that regulate the tumor radiosensitivity quantitatively.

2 Methods

Our approach to obtaining a mesoscale description of the vascular microenvironment combines models of flow and mass transfer characterized by heterogeneous dimensionality. This approach relies on the fact that the lower is the spatial dimensionality of the model, decreasing from 3D, 2D, 1D up to 0D (referring to spatially independent lumped parameter models) the simpler is the mathematical complexity of the model and of the numerical methods required to perform computer simulations. This section presents a mixed-dimensional 3D-1D model that describes blood flow and oxygen transfer from the microvasculature to the

tissue microenvironment.Figure 2 illustrates the modelling strategy and motivates why we define it as a *mesoscale* model. Our modeling approach is also called *mixed-dimensional* 3D-1D because microvessels are represented as one-dimensional channels. As discussed in [6, 31] this approximation significantly simplifies the problem at the computational level.

For the sake of completeness, we first briefly review the blood flow model, already presented in [4, 49, 47]. Then, we focus on the oxygen transfer model, describing in detail the governing equations, discussing how they comply with mass conservation. The general layout of the model, showing the interactions of its components is presented in Figure 1.

Before proceeding, we introduce the general notation adopted from now on. The domain Ω represents a small (sub-millimeter) portion of biological tissue, also named the microenvironment, which is composed of two main regions, the microvascular bed Ω_v and the tissue interstitium Ω_t. We assume that the tissue interstitium behaves as a porous medium. We describe each segment of the vascular network as a cylindrical channel; we denote by Γ the outer surface of Ω_v, R its radius and Λ the centerline of the network. Also, we denote with s the arc length coordinate along this line. For coupling the equations between Ω and Λ, we introduce the Dirac-δ on Λ, defined as follows:

$$\delta_\Lambda(\boldsymbol{x}) = \int_\Lambda \delta(\boldsymbol{x} - \boldsymbol{x}_\Lambda(s))ds\,,$$

where $\boldsymbol{x}_\Lambda(s)$ denotes the paramatrization of the network (for each branch) in terms of the arc length, s. For any regular function φ in Ω, δ_Λ satisfies the follwong property,

$$\begin{aligned}\int_\Omega \delta_\Lambda(\boldsymbol{x})\varphi(\boldsymbol{x})d\Omega &= \int_\Omega \int_\Lambda \delta(\boldsymbol{x} - \boldsymbol{x}_\Lambda(s))\varphi(\boldsymbol{x})dsd\Omega \\ &= \int_\Lambda \int_\Omega \delta(\boldsymbol{x} - \boldsymbol{x}_\Lambda(s))\varphi(\boldsymbol{x})d\Omega ds = \int_\Lambda \varphi(\boldsymbol{x}_\Lambda(s))ds\,,\end{aligned}$$

that is, it formally acts as a restriction operator form Ω to Λ.

The physical quantities of interest are the blood pressure p, the blood velocity $\boldsymbol{u}$ and the concentration of transported oxygen C. They are all defined as fields depending on space (being $\boldsymbol{x}$ the spatial coordinates) and possibly on time t. Furthermore, we denote by the subscript $(*_v)$ their restriction to the vascular bed, and with subscript $(*_t)$ the restriction to the interstitial tissue.

We do not address here the details about the numerical approach used for discretizing and solving the model. We remand the interested reader to the Supplementary Materials and related references [3, 4, 49].

2.1 3D-1D model for microvascular flow

The 3D-1D model for microvascular flow has been detailed in a series of works regarding different features of the model such as: (i) 3D-1D coupling [4]; (ii)

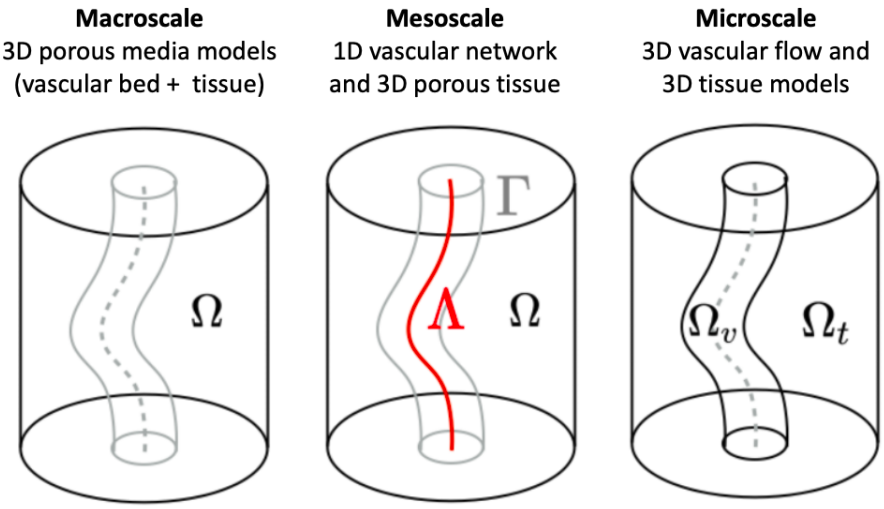

Figure 2: Description of the mesoscale modeling approach, compared to micro and macro-scale strategies. The notation adopted for the vascular and tissue regions is also described.

red blood cell (RBC) transport and RBC dependent rheological properties, described by the Fahraeus-Lindqvist and Zweifach-Fung effects [49]; and (iii) the possible inclusion of lymphatic drainage using a linear or a general non-linear relation with interstitial pressure [47]. The model describes the flow referring to two different domains, namely the interstitial 3D domain (Ω), where the unkowns are the interstitial pressure and velocity $p_t, \boldsymbol{u}_t$ respectively, and the vascular 1D domain (Λ) where the unknowns are blood pressure and velocity $p_v, \boldsymbol{u}_v$. Considering steady flow, exploiting the assumption of very low Reynolds numbers and neglecting gravity, the mass and momentum balance equations for microvascular flow (denoted as $\mathcal{F}$) become the Darcy flow in Ω and a Poiseuille-like flow in Λ:

$$\mathcal{F}: \begin{cases} \boldsymbol{u}_t + \dfrac{\mathrm{K}}{\mu_t}\nabla p_t = 0 & \text{in } \Omega \\ \nabla \cdot \boldsymbol{u}_t + \phi_l - \phi_v \delta_\Lambda = 0 & \text{in } \Omega \\ 8\mu_v u_v + R^2 \partial_s p_v = 0 & \text{in } \Lambda \\ \partial_s(\pi R^2 u_v) + \phi_v = 0 & \text{in } \Lambda \end{cases} \tag{1}$$

where K is the permeability of the porous media, μ is the fluid viscosity, R the vessel radius, ϕ_l the lymphatic drainage, and ϕ_v is the exchange term between the two domains. Precisely, we have $\phi_v = 2\pi R L_p\big((p_v - \overline{p}_t) - \sigma(\pi_v - \pi_t)\big)$ where L_p is the hydraulic conductivity of the vessel wall, π_v and π_t determine the osmotic (or oncotic) pressure gradient across the capillary wall due to the

difference in the concentration of proteins (for example albumin) and σ is the respective reflection coefficient. In the 1D approach, p_v indicates the mean value of the blood pressure on a cross section of a micro-vessel and $\overline{p}_t$ is the mean value of the interstitial pressure computed on the blood/tissue interface of the same cross section. The viscosity of blood within the vascular network has been modeled as

$$\mu_v = \mu_{plasma} \cdot \mu_{eff}(H, D)$$

where the $\mu_{eff}(H, D)$ is defined by the formula presented in [51]:

$$\mu_{eff}(H,D) = \Big[1+(\mu_{0.45}(D)-1)\cdot \frac{(1-H)^{f(D)}-1}{(1-0.45)^{f(D)}-1}\cdot \Big(\frac{D}{D-1.1}\Big)^2\Big]\cdot \Big(\frac{D}{D-1.1}\Big)^2, \quad (2)$$

where $D = 2R$ is the diameter of the vessel, and H is the discharge hematocrit.

The model for microvascular flow is complemented by the one-dimensional RBC transport model (denoted by $\mathcal{H}$) that governs the variation of the discharge hematocrit H in Λ. Such a 1D transport model inherits the steady flow assumption, and it relies on a few other assumptions: (i) transport dominated regime, justified by the large Pe number; (ii) no extravasation and degradation of RBCs; (iii) the network connectivity includes bifurcations and anastomosis solely. The 1D hematocrit transport model is therefore defined as:

$$\mathcal{H}: \ \pi R^2 u_v \partial_s H - \phi_v H = 0 \quad \text{in } \Lambda\,. \quad (3)$$

At vessels junctions, the mass conservation is enforced and, when considering a bifurcation, the RBCs split is computed following the approach reported in [50]. Interested readers may refer to [49] for a more detailed description of $\mathcal{H}$ at junctions and for other details about the numerical discretization of $\mathcal{F}$ and $\mathcal{H}$.

2.2 3D-1D model for oxygen transport

The 3D-1D problem for oxygen transport (named $\mathcal{O}$) employs the solutions from $\mathcal{F}$ and $\mathcal{H}$ to describe blood flow and hematocrit transport. We present the derivation of the model, starting from the description of the physical phenomena involved. Consistently with the previous models, the oxygen transport model is composed by equations in the two domains Λ and Ω.

2.2.1 Oxygen transport in the vascular network.

Oxygen is available in the blood as dissolved oxygen, C_v, and hemoglobin-bound oxygen C_{HbO_2}. The total oxygen concentration, C_v^{tot}, is the sum of the two, namely $C_v^{tot} = C_v + C_{HbO_2}$. Our model relies on three main assumptions: (i) oxyhemoglobin diffusion in the blood is negligible; (ii) the dissolved and hemoglobin-bound oxygen phases are at chemical equilibrium at any time; (iii) absence of oxygen consumption within the blood flow. Then, let us write the following 1D equation for the balance of oxygen fluxes:

$$\pi R^2 \ \frac{\partial}{\partial s}\left(-D_v \frac{\partial C_v}{\partial s} + u_v \ C_v^{tot}\right) + \phi_{O_2} = 0\,, \quad (4)$$

where ϕ_{O_2} accounts for the the interaction with the tissue that will be detailed later on. According to assumption (ii) there exists a relation $C_{HbO_2} = f(C_v)$. To describe such a non-linear relation, we rewrite the bound oxygen concentration as:

$$C_{HbO_2} = N\ C_{Hb}\ S(p_{O_2})\ , \tag{5}$$

where N is the Hüfner factor representing the oxygen binding capacity of human hemoglobin, defined as the amount of oxygen per unit of hemoglobin, measured in ml_{O_2}/g_{Hb}; C_{Hb} is the hemoglobin concentration in the blood and $S(p_{O_2})$ is the hemoglobin saturation with oxygen. Then, the factor C_{Hb} is estimated as $C_{Hb} = H\ MCHC$, where H is the hematocrit and $MCHC$ is the Mean Corpuscular Hematocrit Concentration, a physiological parameter that represents the amount of hemoglobin in each RBC, expressed in g_{Hb}/ml_{RBC}. The saturation $S(p_{O_2})$, is well described by the Hill equation:

$$S(p_{O_2}) = \frac{(p_{O_2})^\gamma}{(p_{O_2})^\gamma + (p_{s_{50}})^\gamma}\ , \tag{6}$$

where $p_{s_{50}}$ is the oxygen partial pressure at hemoglobin half-saturation and γ is the Hill exponent. The term $p_{s_{50}}$ depends on [7, 71]: (i) the temperature, in °C; (ii) the pH inside RBCs through the Bohr effect; (iii) the CO_2 partial pressure through the Haldane effect; (iv) the 2,3-Bisphosphoglyceric acid concentration (or 2,3-DPG), a protein that reduces the affinity of the hemoglobin to oxygen. We selected from literature the values for all these parameters, assuming them to be constant in time and uniform in space. To estimate the oxygen partial pressure at half-saturation, we applied an empirical equation from Kelman's model ([7]):

$$p_{s_{50}} = 26.8 \cdot 10^{(0.4\ (7.24-pH)+0.06\ log(\frac{p_{CO_2}}{40})+0.024\ (T-37))}\ .$$

We apply the Henry's equation, namely, $C = \alpha\ P$ where C is the concentration of a gas in a solution with partial pressure P, and α is the solubility coefficient of that gas depending on the temperature, T [°C], to (6) so that we obtain $S(C_v)$ as follows,

$$S(C_v) = \frac{C_v^\gamma}{C_v^\gamma + (\alpha_{pl}\ p_{s_{50}})^\gamma}\ . \tag{7}$$

Finally, combining equations (4), (5), and (7), we obtain the equation governing the 1D oxygen transport within the vasculature:

$$-\pi R^2\ D_v \frac{\partial^2 C_v}{\partial s^2} + \pi R^2 \frac{\partial}{\partial s}\left(u_v\ C_v + u_v\ k_1\ H\ \frac{C_v^\gamma}{C_v^\gamma + k_2}\right) = -\phi_{O_2} \quad \text{on } \Lambda\ , \tag{8}$$

where, for simplicity of notation, we set $k_1 = N\ MCHC$ and $k_2 = (\alpha_{pl}\ p_{s_{50}})^\gamma$. We also observe that equation (8) can be formally rewritten in the standard form of an advection-diffusion equation, using a modified velocity field,

$$u_{v,O_2} = u_v\left(1 + k_1\ H\ \frac{C_v^{\gamma-1}}{C_v^\gamma + k_2}\right)\ .$$

2.2.2 Oxygen transfer.

To describe how the oxygen is delivered to the tissue, the flux ϕ_{O_2} has to be detailed. We model the vascular wall as a semipermeable membrane, see for example, [25]. As a result, the total oxygen flux across the membrane can be split into the sum of diffusive flux, $\phi_{O_2}^{diff}$, and convective flux, $\phi_{O_2}^{adv}$, namely $\phi_{O_2} = \phi_{O_2}^{diff} + \phi_{O_2}^{adv}$. In a 1D model of the microvessels, we describe the fluxes that leave each cross section of the channels as follows:

$$\phi_{O_2}^{diff} = 2\pi R\ P_{O_2}(C_v - \overline{C}_t), \quad \phi_{O_2}^{adv} = (1 - \sigma_{O_2})\ \left(\frac{C_v + \overline{C}_t}{2}\right)\ \phi_v, \tag{9}$$

where P_{O_2} is the permeability of the vascular wall to oxygen, σ_{O_2} is a reflection coefficient relative to the oxygen molecule. As previously denoted for the pressure, C_v indicates the mean value of the oxygen concentration on a cross section of a micro-vessel $\overline{C}_t$ the mean value of the interstitial oxygen concentration computed on the blood/tissue interface of the same cross section.

2.2.3 Oxygen transport within the tissue.

Oxygen can diffuse within the interstitial space, it can be transported by the movement of the interstitial fluid, and it can be depleted by the cells. These well-known phenomena can be described by using the general diffusion-advection-reaction equations applied to the domain Ω, that is:

$$-\nabla \cdot (-D_t \nabla C_t + \mathbf{u}_t\ C_t) = \phi_{O_2}\, \delta_\Lambda - \phi_m \quad \text{on } \Omega, \tag{10}$$

where C_t is the interstitial oxygen concentration, D_t is oxygen diffusion coefficient, $\mathbf{u}_t$ the fluid velocity. At the right hand side, we observe the net balance between the oxygen delivered to the tissue per unit length of the vascular network, multiplied by δ_Λ (a linear distribution of Dirac δ-functions on Λ) used to transform it into a volume flux, and the oxygen consumption term per unit volume of the tissue, denoted as ϕ_m.

Oxygen depletion by the metabolic activity of the tissue is described by the Michaelis-Menten formula [37]:

$$\phi_m(p_{O_2}) = V_{max}\ \frac{p_{O_2}}{p_{O_2} + p_{m_{50}}} \tag{11}$$

where V_{max} is the maximum consumption rate of oxygen in the intersitial tissue expressed in $(ml_{O_2}/cm^3)/s$, p_{O_2} is the oxygen partial pressure within the tissue, and $p_{m_{50}}$ is the oxygen partial pressure at half consumption rate, also known as Michaelis-Menten constant. Since the model uses oxygen concentration instead of oxygen partial pressure, the Michaelis-Menten formula has been written leveraging Henry's equation. We set the temperature at 37°C and as a consequence the Michaelis-Menten formula can be transformed as follows,

$$\phi_m(C_t) = V_{max}\ \frac{C_t}{C_t + \alpha_t\ p_{m_{50}}}\ . \tag{12}$$

2.2.4 The coupled oxygen model.

Equation (13) is the 3D-1D oxygen model, denoted with $\mathcal{O}$. It is composed by joining equations (10), (12), (8) and (9):

$$\mathcal{O}: \begin{cases} \nabla \cdot (-D_t \nabla C_t + \mathbf{u}_t \; C_t) + V_{max} \; \dfrac{C_t}{C_t + \alpha_t \; p_{m_{50}}} = \phi_{O_2} \, \delta_\Lambda \quad \text{on } \Omega \\ \pi R^2 \dfrac{\partial}{\partial s} \left(-D_v \dfrac{\partial C_v}{\partial s} + u_v \; C_v + u_v \; k_1 \; H \; \dfrac{C_v^\gamma}{C_v^\gamma + k_2} \right) = -\phi_{O_2} \quad \text{on } \Lambda \\ \phi_{O_2} = 2\pi R \; P_{O_2} (C_v - \overline{C}_t) + (1 - \sigma_{O_2}) \; \left(\dfrac{C_v + \overline{C}_t}{2} \right) \; \phi_v \quad \text{on } \Lambda \\ C_v = C_{in} \quad \text{on } \partial\Lambda_{IN} \\ -D_v \dfrac{\partial C_v}{\partial s} = 0 \quad \text{on } \partial\Lambda_{OUT} \\ -D_t \nabla C_t \cdot \mathbf{n} = \beta_{O_2} \; (C_t - c_{0,t}) \quad \text{on } \partial\Omega \end{cases} \tag{13}$$

Such a model is complemented with a set of boundary conditions to complete the description of the problem. We set different boundary conditions for the two domains. First, at the vascular inlets, marked as $\partial\Lambda_{IN}$, we specify the oxygen concentration. Conversely, at the vascular endpoints marked as $\partial\Lambda_{OUT}$, null diffusive flux is enforced. For the tissue, we simulate the presence of an adjacent tissue domain with a boundary conductivity β_{O_2} and a far-field concentration c_0.

2.2.5 Mathematical model of the vascular junctions and mass conservation

Model (13) describes the behavior of any portion of the vascular network Λ, but it does not addresses the balance of the oxygen at the junctions between microvessels (bifurcations or anastomoses). This is an essential but delicate aspect of the problem. On one hand, it governs the global mass conservation properties; on the other hand, it requires to blend the governing equations in the microvessels with the mass balance equations at the junctions. This step is naturally achieved at the level of the weak formulation of the problem that is introduced in what follows.

Let us integrate the oxygen transport problem over Ω_v and multiply it by a smooth test function, q_v. We remark that the integration over the network Λ should be split into the integrals on each branch, denoted with Λ_i with $i = 0, \ldots, N$. Then, we integrate by parts the diffusion term on each branch to distribute the second derivative of C_v on the test function. Through these

steps, the diffusion term is transformed as follows:

$$
\begin{aligned}
-\int_{\Lambda} \pi R^2 D_v \ \frac{\partial^2 C_v}{\partial s^2} q_v \, d\Lambda &= -\sum_{i=0}^{N} \int_{\Lambda_i} \pi R_i^2 D_v \frac{\partial^2 C_v}{\partial s^2} q_v \, d\Lambda_i \\
&= \int_{\Lambda} \pi R^2 D_v \ \frac{\partial C_v}{\partial s} \frac{\partial q_v}{\partial s} \, d\Lambda - \sum_{i=0}^{N} \pi R_i^2 \left[D_v \frac{\partial C_v}{\partial s} q_v \right]_{\Lambda_i^-}^{\Lambda_i^+} .
\end{aligned}
$$

where Λ_i^- and Λ_i^+ represent the input and output endpoints of i-th branch, Λ_i. By putting all the terms together, the weak form of equation (13)-b reads as follows:

$$
\begin{aligned}
&\int_{\Lambda} \pi R^2 D_v \ \frac{\partial C_v}{\partial s} \frac{\partial q_v}{\partial s} \, d\Lambda + \int_{\Lambda} \pi R^2 u_v \ C_v q_v \, d\Lambda \\
&\qquad + \int_{\Lambda} \left[2\pi R \ P_{O_2} (C_v - \overline{C}_t) + \frac{1}{2} (1 - \sigma_{O_2}) \ \phi_v \left(C_v + \overline{C}_t \right) \right] q_v \, d\Lambda \\
&\qquad\qquad - \sum_{i=0}^{N} \pi R_i^2 \left[D_v \frac{\partial C_v}{\partial s} q_v \right]_{\Lambda_i^-}^{\Lambda_i^+} = 0 \quad (14)
\end{aligned}
$$

Let Φ be the total mass flow rate along a capillary, expressed by the sum of convective mass flow rate and diffusive mass flow rate,

$$
\Phi = \pi R^2 u_v C_v^{tot} - \pi R^2 D_v \ \frac{\partial C_v}{\partial s}
$$

Let us consider a junction of three micro-vessels (bifurcation or anastomosis) numbered as $i = 0, 1, 2$ where the index 0 represents the parent vessel and $1, 2$ are the daughter vessels. Mass conservation at junctions can be expressed as

$$
\Phi_0 = \Phi_1 + \Phi_2 \, . \quad (15)
$$

We assume that the free oxygen concentration is continuous at the junction, but the oxyhemoglobin concentration depends on hematocrit and velocities which may exhibit a jump at the junction points. As a result, the enforcement of (15) into (13) is not a trivial task. It is achieved by combining (15) with the corresponding relations for blood flow and hematocrit. The blood flow and hematocrit models, (1) and (3) ensure that the following balances are satisfied at the junction:

$$
\begin{aligned}
\text{fluid mass balance,} \qquad & \pi R_0^2 u_{v_0} = \pi R_1^2 u_{v_1} + \pi R_2^2 u_{v_2} \, ; \\
\text{haemtocrit mass balance,} \qquad & \pi R_0^2 u_{v_0} H_0 = \pi R_1^2 u_{v_1} H_1 + \pi R_2^2 u_{v_2} H_2 \, .
\end{aligned}
$$

To enforce the balance of total oxygen concentration at the junctions, we first multiply the flow rate conservation by the free oxygen concentration, that is continuous at the junctions:

$$
\pi R_0^2 u_{v_0} C_{v_0} = \pi R_1^2 u_{v_1} C_{v_1} + \pi R_2^2 u_{v_2} C_{v_2} \, . \quad (16)
$$

As the saturation $S(C_v)$ directly depends on the free oxygen concentration, it is also continuous at the junctions. Then, we multiply the hematocrit conservation by the saturation equation:

$$\pi R_0^2 u_{v_0} H_0 \; S(C_{v_0}) = \pi R_1^2 u_{v_1} H_1 \; S(C_{v_1}) + \pi R_2^2 \, , u_{v_2} H_2 \; S(C_{v_2}) \tag{17}$$

and we rewrite the (17) in terms of oxyhemoglobin concentration, Ψ:

$$\pi R_0^2 u_{v_0} \Psi_0 = \pi R_1^2 u_{v_1} \Psi_1 + \pi R_2^2 u_{v_2} \Psi_2 \, . \tag{18}$$

Finally, we sum the (16) and the (18) and we apply the definition of total oxygen concentration:

$$\pi R_0^2 u_{v_0} C_{v_0}^{tot} = \pi R_1^2 u_{v_1} C_{v_1}^{tot} + \pi R_2^2 u_{v_2} C_{v_2}^{tot} \, . \tag{19}$$

Equation (19) demonstrates the conservation of total oxygen concentration by combining mass balance equations of different variables. Then, replacing (19) into (15), we obtain that the diffusive fluxes satisfy an independent balance law:

$$-D_v \; \frac{\partial C_{v_0}}{\partial s} = -D_v \; \frac{\partial C_{v_1}}{\partial s} - D_v \; \frac{\partial C_{v_2}}{\partial s} \, . \tag{20}$$

As balance at the junctions is already satisfied for all previously considered variables (namely blood flow rate, discharge hematocrit, oxyhemoglobin concentration), the oxygen diffusive flux balance stated in (20) is the only missing component to be addressed. Going back to the variational formulation of oxygen transport in the vascular network (14), for a bifurcation or anastomosis (where the summation from $i = 0$ to $i = N = 2$ spans over the parent and daughter branches) we see that (20) can now be easily enforced as follows,

$$\begin{aligned} \sum_{i=0}^{N} \pi R_i^2 \left[D_v \frac{\partial C_v}{\partial s} q_v \right]_{\Lambda_i^-}^{\Lambda_i^+} &= \sum_{i=0}^{N} \pi R_i^2 \left[D_v \frac{\partial C_v}{\partial s} \right]_{\Lambda_i^-}^{\Lambda_i^+} q_v \\ &= \pi R^2 \; \left[D_v \frac{\partial C_v}{\partial s} \; q_v \right]_{\partial \Lambda_{OUT}} - \pi R^2 \; \left[D_v \frac{\partial C_v}{\partial s} \; q_v \right]_{\partial \Lambda_{IN}} \, . \end{aligned}$$

Owing to the boundary conditions for C_v of system (13), the last two terms of the previous equation vanish, because $\dfrac{\partial C_v}{\partial s} = 0$ on $\partial \Lambda_{OUT}$ and $q_v = 0$ on $\partial \Lambda_{IN}$, as Dirichlet boundary conditions are enforced at the inflow. As a result, the governing equation for free oxygen in the vascular bed, including mass conservation at the junctions, becomes,

$$\begin{aligned} &\int_\Lambda \pi R^2 D_v \; \frac{\partial C_v}{\partial s} \frac{\partial q_v}{\partial s} \, d\Lambda + \int_\Lambda \pi R^2 u_v \; C_v q_v \, d\Lambda \\ &\quad + \int_\Lambda \left[2\pi R \; P_{O_2} (C_v - \overline{C}_t) + \frac{(1 - \sigma_{O_2})}{2} \; \phi_v \left(C_v + \overline{C}_t \right) \right] q_v \, d\Lambda = 0 \, . \end{aligned} \tag{21}$$

We proceed similarly for the tissue equation, moving along the classical steps as there is no need to address the junctions there. We denote by q_t the test function on Ω, by $\left(\cdot,\cdot\right)_*$ the inner product over the domain $*$, and by u_{v,O_2} the modified fluid velocity comprising the hemoglobin term (see equation (8) and also the Supplemetary material). Therefore, the whole weak formulation of the oxygen transport problem results to be:

$$\mathcal{O}: \begin{cases} (D_t \nabla C_t,\ \nabla q_t)_\Omega + (\nabla \cdot (\mathbf{u}_t C_t),\ q_t)_\Omega + (\beta_{O_2} C_t, q_t)_{\partial\Omega} \\ \qquad - \left(\left[2\pi R\ P_{O_2}(C_v - \overline{C}_t) + \frac{(1-\sigma_{O_2})}{2}\ \phi_v\ \left(C_v + \overline{C}_t\right) \right], \overline{q}_t \right)_\Lambda \\ \qquad + \left(\frac{V_{max}}{C_t^{(k-1)} + \alpha_t p^{m_5 0}}\ C_t,\ q_t \right)_\Omega = (\beta_{O_2} c_{0,t}, q_t)_{\partial\Omega}\,, \\ \\ \left(\pi R^2 D_v\ \dfrac{\partial C_v}{\partial s}, \dfrac{\partial q_v}{\partial s} \right)_\Lambda + \left(\pi R^2 u_{v,O_2}\ C_v, q_v \right)_\Lambda \\ \quad + \left(\left[2\pi R\ P_{O_2}(C_v - \overline{C}_t) + \frac{(1-\sigma_{O_2})}{2}\ \phi_v \left(C_v + \overline{C}_t\right) \right], q_v \right)_\Lambda = 0\,. \end{cases} \tag{22}$$

3 Results

We apply the model to different vascular geometries, from the simplest, that is a single branch, to relatively complex and realistic vascular networks. For completeness, some numerical tests on a bifurcation and anastomosis are discussed in the Supplementary Materials.

The parameters used for the following simulations are reported in Table 1. More precisely, we report two sets of values. The first ones are taken from [49] and will be used for the simulations of 3.1. The second ones are used in section 3.2 for comparison with [59]. For the boundary conditions in the following tests, we have used the values reported in Table 1 (the last three rows).

We employ the finite element method to discretize the problem, and we use a fixed point method to linearize the equations containing nonlinear factors. The discrete problem is initialized and solved by an *in-house* code developed using the GetFem++ library, see [12]. When the first version of the code was written, for the development of [6], GetFem++ library was particularly appealing because of the ability to discretize and couple operators across dimensions, i.e. 3D, 2D, 1D, and for the integration tools on manifolds that do not conform with the computational mesh. We are aware that other open access finite element libraries may now offer similar tools. Full details of the discretization and solving procedure can be found in the supplementary materials.

Table 1: Physiological parameters used for the numerical tests.

SYMBOL	PARAMETER	UNIT	SET #1	REF.#1	SET #2	REF.#2
D	characteristic length	m	5×10^{-4}	[49]	1.60×10^{-4}	[59]
R	average radius	m	4×10^{-6}	[49]	–	–
K	tissue hydraulic conductivity	m^2	1×10^{-18}	[28, 49]	7.68×10^{-18}	[61]
μ_t	interstitial fluid viscosity	cP	1.2	[49]	1.2	[49]
μ_v	blood viscosity	cP	9.33	[49]	computed	(2)
L_p	wall hydraulic conductivity	$m^2\,\mathrm{s\,kg^{-1}}$	–	–	2.70×10^{-12}	[61]
$\delta\pi$	oncotic pressure gradient	$mmHg$	–	–	10	[24]
σ	reflection coefficient	$-$	–	–	0.95	[26]
σ_{O_2}	O_2 reflection coefficient	$-$	–	–	0	[59]
P_{O_2}	O_2 wall permeability	m/s	3.5×10^{-5}	[3, 28]	4.75×10^{-4}	[59]
D_v	vascular diffusion coefficient	m^2/s	2.18×10^{-9}	[34]	2.18×10^{-9}	[34]
$N \times MCHC$	max. hemoglobin-bound O_2	ml_{O_2}/ml_{RBC}	–	–	0.5	[59]
γ	Hill constant	–	–	–	3	[59]
p_{s50}	O_2 at half-saturation	$mmHg$	–	–	38	[59]
α	O_2 solubility coefficient	ml_{O_2}/ml	–	–	3.1×10^{-5}	[59]
D_t	tissue diffusion coefficient	m^2/s	2.41×10^{-9}	[34]	1.94×10^{-9}	[59]
V_{max}	O_2 consumption rate	$ml_{O_2}/cm^3/s$	6.17×10^{-5}	[72]	2.33×10^{-3}	[59]
p_{m50}	Michaelis-Menten constant	$mmHg$	–	–	1	[57]
Q	total inlet flow rate	ml/s	–	–	1.8×10^{-7}	[59]
$p_{O_2,in}$	O_2 partial pressure at inlets	$mmHg$	96	[29]	50	[59]
H_{in}	Discharge hematocrit at inlets	–	–	–	0.5	[57]
β_{O_2}	Boundary conductivity	$m^2\ s/kg$	0.0	[29]	0.0	[59]

3.1 Oxygen transfer applied to simple benchmarks

3.1.1 Single branch benchmark and the Krogh's model.

This test case consists of a single rectilinear cylindrical vessel immersed in a cubic tissue slab with homogeneous properties. In such conditions, the Krogh's model for oxygen transfer can also be applied [29]. For validation purposes

and to highlight the additional features of the proposed model, we compare the results of the two.

The Krogh's model is based on a generic advection-diffusion-reaction equation for the tissue domain and the flow rate and oxygen balance in the bloodstream for an infinitesimal longitudinal section of one microvessel. The oxygen concentration in the tissue is represented in cylindrical coordinates $C(r, z, \vartheta)$. Under the assumptions of axial-symmetry and steady-state, negligible axial diffusion in the tissue, and uniform oxygen consumption rate, the Krogh's model reduces to a system of ordinary differential equations along the radial direction in the tissue and the axial direction along the vascular centerline. Such equations can be solved analytically and compared to the numerical solution of model (13).

Besides the values reported in Table 1 (set #1), for Krogh's model we choose the length of the vessel d equal to $5 \times 10^{-4}\, m$, the axial velocity on the vessel $u_v = 0.2\, m/s$ and the ratio between outer and inner radius equal to 25. The boundary conditions have been chosen following the Krogh's model, namely the oxygen concentration at the inlet is set to $p_{O_2,in}$, and zero diffusion flux is set at the outlet of the vessel. The fluid dynamic problem has been solved imposing a pressure gradient of $3.5 mmHg$ between the inlet and outlet of the vessel, in particular $p_{O_2,in}$ set to 32 $mmHg$ and $p_{O_2,out}$ set to 28.5 $mmHg$ to reproduce the conditions specified in [47]. We point out that this test case doesn't represent well the real microvascular conditions, because the physiological vascular surface to volume ratio is not respected.

We compare the Krogh's model with a simplified version of model (13), where the convective velocity in the tissue and across the vascular wall is neglected, namely, $\boldsymbol{u}_t = \mathbf{0}$ and $\phi_v = 0$ and also the tissue consumption term is set to be constant, that is $\phi_m(C_t) = V_{max}$ in equation (12). As a result, this test highlights the differences in oxygen distribution due to the endothelial resistance solely. The results of this comparison are shown in Figure 3. The left panel of Figure 3 shows that the vascular concentration of free oxygen is very similar in the two cases, as expected since the models are equivalent is this region. The main differences are visible in the tissue, reported on the right panel, where the oxygen concentration calculated with the simplified version of model (13) is visibly lower than in the Krogh's case. This behavior is due to the diffusive exchange term, $\phi_{diff} = 2\pi R\ P_{O_2}(C_v - \overline{C}_t)$ of equation (9). In contrast to (9), Krogh's equations impose continuity between the concentration at the capillary wall and in the tissue. In this way, the resistance of the endothelium to oxygen transfer is neglected, which justifies the higher value of oxygen concentration predicted by Krogh's model. This interpretation of the results is confirmed, observing that for higher oxygen permeability the differences between (13) and Krogh's decrease in the tissue.

3.2 A comparative study on a realistic scenario

As previously observed, the characteristic trait of the proposed model is its ability to embrace different phenomena, such as variable blood viscosity, intramural

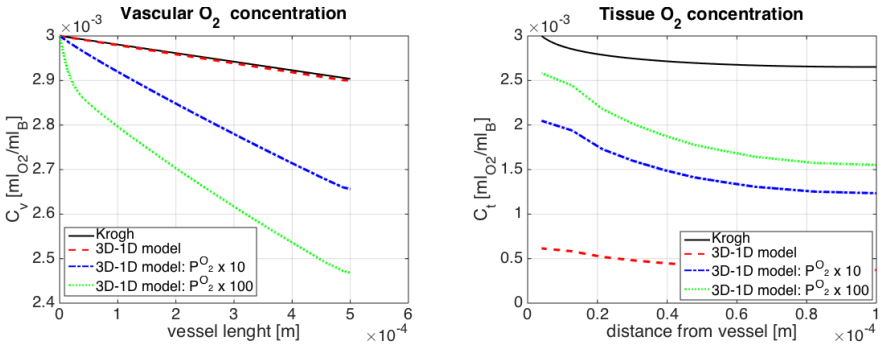

Figure 3: The left panel shows the free oxygen concentration in the vessel modeled by Krogh's equations (continuous line) and simplified version of model (13) for various permeability coefficients (dotted lines, described in the legend). The right panel shows the distribution of oxygen concentration in the tissue along the radial direction starting from the mid-point of the vessel, for various permeability coefficients.

and interstitial transport, mass transport with diffusive and advective effects.

The microvascular flow model has been validated by the authors in previously published works. For example in [49], the authors have extensively compared the simulations based on (1) with analytical solutions, as a verification of the correct discretization of the equations. More importantly, in [30] (see in particular Table 1), the authors and co-workers have compared the outcome of model (1) (obtained using a tissue slab of 540 $\times$ 740 $\times$ 400 μm in which is embedded a network of 28 branches of diameters ranging from 56.4 to 18.8 μm, similar but not equivalent to the one analyzed here), with the data provided in [46], Table 1 (for the category of arterioles). As it can be verified, the predictions on velocity, Reynolds number, wall shear stress, and apparent viscosity, are in excellent agreement with the measured data. Authors further compared the computational results with experimental data from microvascular networks cultured on-a-chip (width = 3 mm, height = 500 μm) reporting a good agreement in terms of interstitial fluid velocity (1-2 μm/s, see figure 4 in [42]). Concerning oxygen transoprt, from a general standpoint, our results in terms of tissue oxygen partial pressure also agree with values reported in the literature for the brain tissue, namely 6-25 mmHg measured in [54, 73].

For a more precise validation of the model and to assess the relative importance of these effects on the total amount and the spatial distribution of oxygen in the microvascular environment, we address a comparative study of our model with previously published results in [59]. In particular, we use the realistic microvasculature obtained from [57] and freely available online. It represents a voxel of 150 $\times$ 160 $\times$ 140 μm containing 50 microvessels. In what follows it will be simply called the *rat brain dataset*. The dataset also reports the specification of the inflow vessels (visualized in Figure 4 with arrows on the right panel) with

the corresponding flow rates. For the simulations described in this section, the pressure values are prescribed at the boundary of the network. To conform to the prescribed data and obtain a fair comparison, we have manually tuned the prescribed pressure at the inflow points to match the rat brain flow rate in the dataset.

We observe that the oxygen transport model presented in [59] and applied to this case (among other scenarios), encompasses almost all the phenomena considered here except for the convective terms for intramural transport as well as the convective terms in the interstitial volume. For validation purposes, we switch off these effects in our model, and we compare the results of simulations with the ones already published. We also compare the complete formulation of our model with the previous results.

The parameters for this test case are taken from Tables 1 (dataset #2). To switch off the intramural and interstitial convective effects, we set L_p to zero. By choosing $\beta_{O_2} = 0$, the conditions at the boundary of the interstitial volume (i.e., the boundary of the voxel with the exterior) are consistent with the *pointwise no-flux solution* of [59].

Table 2 of [59] reports the percent of the volume that falls below a given oxygen partial pressure. We calculate the corresponding quantities for our model, and we report the comparison in Table 2. We observe an excellent agreement between the estimated hypoxic fraction calculated by the two models when only the diffusive phenomena govern the oxygen transport. As oxygen is a very small molecule, diffusion is expected to prevail on transport phenomena. This is confirmed by the third row of Table 2 that reports the calculated hypoxic volume fractions when convective transport phenomena are switched on. We point out that, for oxygen levels, the results are also insensitive to the choice of boundary conditions for the artificial boundaries of the fluid model (1).

Table 2: Estimated hypoxic fraction for the rat brain model.

	($\leq$ 1 mmHg)	($\leq$ 3 mmHg)	($\leq$ 5 mmHg)
Table 2 of [59]	7.4%	13.9%	20.2%
This model $L_p = 0$	9.0%	15.7%	22.1%
This model $L_p \neq 0$	9.0%	15.7%	22.1%

Finally, Figure 4 reports the variation of p_{O_2}, C_v and C_v^{tot} along the microvascular network. All these variables change significantly along the vessels. As expected, they all decrease in average moving from the inflow to the network's outflow points. The first two are directly proportional due to Henry's law. The third one is connected to the previous through the saturation function, and affected by H.

3.3 The sensitivity of oxygen distribution with respect to vascular hematocrit and oxygen consumption

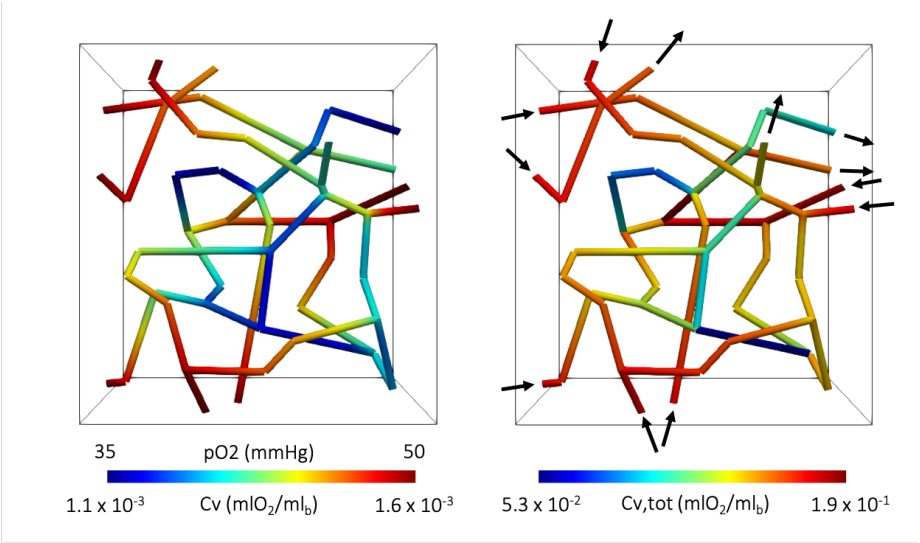

Figure 4: Visualisation of p_{O_2}, C_v and C_v^{tot} along the microvascular network.

A sensitivity analysis for problem (1) has been addressed in a previoius work [48]. There, the authors quantify the influence of some parameters of Table 1 (precisely $L_p, \sigma, \delta\pi, H_{in}$ among others) on the quantities $p_v, u_v, p_t, \boldsymbol{u}_t$ computed by the model (1). Table 3 of [48] shows that the paramaters that determine the fluid exchange between the blood and the interstitial fluid are among the most relevant. Here, we complement the results of [48] with a much simpler sensitivity study, relative to the parameters that regulate the oxygen transfer from blood to tissue. We identify a parameter space made of two entries: (i) the inlet hematocrit H_{in} that determines the inlet boundary conditions of (3) (see [49] for more details) and (ii) the oxygen consumption rate in the tissue V_{max}. For simplicity, we only analyze the corner points of the parameter space, which correspond to the four possible combinations of low/normal values of H_{in} and V_{max}. For the normal values of these parameters we take $H_{in} = 50\%$ and V_{max} as in Table 1 (set #2). For low values, we divide both of a factor 2. The cases $H_{in} = 25\%$ and $V_{max}/2$ aim at representing a poorly oxygenated and dysfunctional tissue, respectively, which could be considered a typical vascularization in a tumor.

Besides analyzing the distribution maps of the oxygen partial pressure, we report quantitative indicators such as (i) the blood flow rate at the inflow of the vasculature, called IFR and measured in $[mm^3/s]$; (ii) the oxygen flow rate at the inflow, called IFR_{O_2} measured in $[ml_{O_2}/s]$; (iii) the net filtration rate of plasma leaking through the vascular/tissue interface, called NFR, measured in $[\mu l/s]$; (iv) the oxygen net filtration rate through the vascular/tissue interface, named NFR_{O_2} measured in $[ml_{O_2}/s]$ (i.e. the total net flux of oxygen crossing the vascular wall); (v) and the interquartile range, named IQR of the calculated

Table 3: Input and output values of the different scenarios. The input parameters that are arbitrarily varied are reported in the first two columns. The other columns show the calculated output values, as described in the text, see items (i) to (vi).

	H_{in}	V_{max}	IFR	IFR_{O2}	NFR	NFR_{O2}	IQR p_{O_2}	M p_{O_2}
A	0.5	2.33E-03	1.80E-04	3.19E-08	7.55E-08	6.51E-09	13.25	12.28
B	0.5	1.17E-03	1.80E-04	3.19E-08	7.55E-08	3.70E-09	9.12	28.20
C	0.25	2.33E-03	3.31E-04	2.96E-08	7.44E-08	6.47E-09	12.98	11.80
D	0.25	1.17E-03	3.31E-04	2.96E-08	7.44E-08	3.69E-09	9.12	27.75

oxygen values (precisely the oxygen partial pressure p_{O_2} sampled at the computational grid points and measured in $[mmHg]$) that is a measure of statistical dispersion defined as the difference between 75^{th} and 25^{th} percentiles; (vi) the median of the oxygen distribution at the same points measured in $[mmHg]$. The IQR/median indicators are interesting because they evidence the variations of the oxygen spatial distribution.

We have performed numerical simulations with the four different input values shown in the first two columns of Table 3. The output parameters (i)-(vi) computed in these scenarios are reported in the remaining six columns. Furthermore, to better visualize the correlations between inputs and outputs, we have normalized each column with respect to the reference value of the first row and plot the corresponding table in Figure 5. This figure shows that some output variables are positively correlated with the inputs, some are negatively correlated, and some are not significantly correlated. The interpretation of these results will be discussed in the next section.

Finally, the oxygen partial pressure maps in the vasculature and the tissue are visualized in Figure 5, together with the quantification of the indicators described above.

4 Discussion

The results presented in the first and second part of the previous section confirm the validity of the proposed model, its numerical discretization, and the corresponding software implementation. We remark that Krogh's model relies on different governing principles than ours. In particular, the endothelial resistance to oxygen transfer is neglected and the equilibrium between the oxygen radial concentration gradients and tissue consumption is directly enforced in the model, rather than being a consequence of balance principles. Conversely, when comparing the model with the results of [59], excellent quantitative agreement is observed. Furthermore, the simulations of Table 2 confirm that the oxygen transport from the microvessels to the interstitial tissue is diffusion dominated.

The third part of section 3, investigates the sensitivity of the proposed model with respect to the main factors of the oxygen transfer pipeline, from the in-

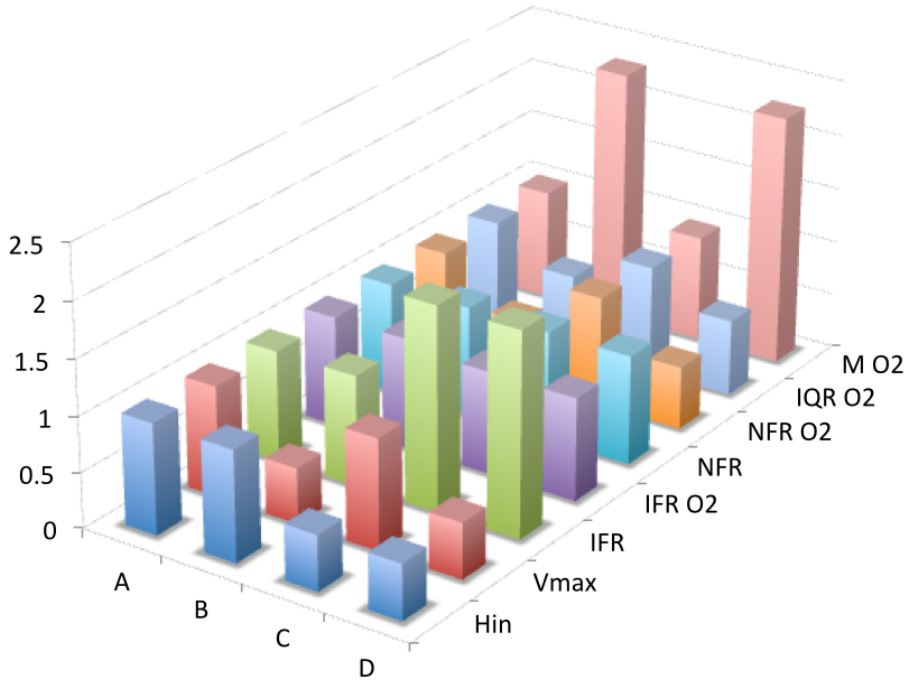

Figure 5: A graphical representation of Table 3 after normalization of the table with respect to the first row, i.e. case A (for this reason all the columns in the first row are equal to the unity).

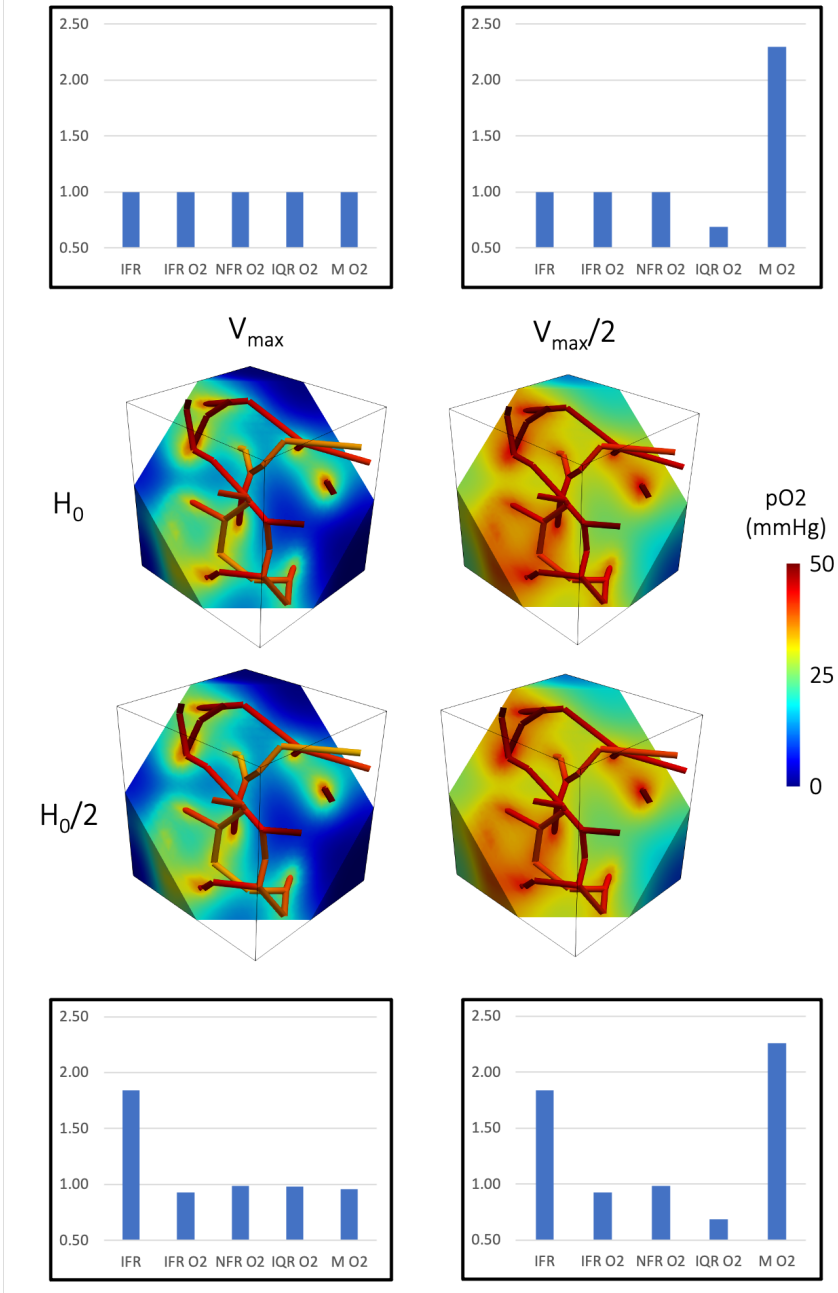

Figure 6: Visualization of the oxygen partial pressure maps in the vasculature and in the tissue, in the four scenarios (named as A,B,C,D) of Table 3. Above and below each case, we report the quantification of the indicators (i)-(vi) using a bar-chart.

put (i.e., the hematocrit level) to the output (i.e., the oxygen consumption). From the visualization of Figure 5 we observe some important effects emerging from the interaction of flow, hematocrit and oxygen transport that should be discussed. We see that the blood inflow rate in the system is highly affected by the variation of hematocrit, with a clear negative correlation. Keeping in mind that the vascular pressure drop from inflow to outflow endpoints of the network is fixed, this effect can be justified by the influence of hematocrit on viscosity. However, we see that the corresponding oxygen inflow rate is much less sensitive to decreasing the parameter H_{in}, as a proportional increase of IFR compensates this variation. Looking at the net filtration rates through the vascular wall, we observe an opposite behavior, as NFR is insensitive to the variation of the inputs while NFR_{O_2} positively correlates with V_{max}. The more oxygen consumption occurs in the interstitial volume, the more oxygen will cross the vascular/tissue interface. Then, if we identify the *oxygenation* of the tissue with the mean value (precisely the median) of the oxygen in the interstitial volume, we expect it to be determined by the competition between the net flux to the tissue and the oxygen consumption by the cell activity. The results of Figure 5 show that, although their relative variation is comparable, the median of the oxygen distribution in the tissue is strongly affected by V_{max} that clearly dominates over NFR_{O_2}. In other words, the availability of oxygen in the tissue turns out to increase significantly when the oxygen consumption in the tissue is decreased. Concerning the oxygen spatial distribution, quantified by IQR_{O_2} and visualized in the partial pressure maps of Figure 5, we see that it negatively correlates with the oxygen median. Although the local oxygen distribution is strongly affected by the vasculature geometry in agreement with previous studies [48], it appears that low oxygen level scenarios exhibit stronger spatial gradients, while a more uniform distribution characterizes scenarios with higher oxygenation.

In this work, we focused on the oxygen exchanges occurring at the microvascular level. To this aim, we have considered the dissolved oxygen, its uptake by the tissue, the interaction with the hemoglobin, and the effect of the microvascular network geometry. Such effects are considered among the most important in this context [44]. Our model also embraces the Zweifach-Fung effect [49, 52, 56], the influence of microvascular network geometry on the microvascular flow [48], and the effect of the pH and the partial pressure of carbon dioxide on hemoglobin saturation, which are often considered when modeling oxygen transport [5, 13, 28, 33, 62].

Recently, other phenomena have been considered to affect the oxygen transport, such as the presence of other related species (nitric oxide, superoxide, myoglobin) [9, 44], the erythrocyte-associated transient fluctuation of p_{O_2} [44], the vasomotor regulation [39, 44], and involvement of arterioles in oxygen exchanges [39]. However, for some of these other phenomena, the mechanism and the role in oxygen transport are still debated, for this reason we don't address them in the proposed model yet.

4.1 Impact of the model on radiotherapy

Concerning future application to radiotherapy, the hypoxic condition characterizes many solid cancers [69]. Hypoxia is known to characterize aggressive and immunosuppressive tumors, being associated with genomic instability, apoptosis, angiogenesis, metastasis and invasion, and metabolic reprogramming [35]. Further, the *oxygen effect*, highlighted in preclinical studies, is of particular relevance for radiotherapy, resulting from oxygen's chemical properties [18, 55, 1]. For cells subjected to ionizing radiation, double-stranded breaks in the DNA helix represent the main lethal event. These breaks are the consequences of the direct effect of radiation depositing its energy on DNA strands and of the indirect effect of free radicals resulting from the radiolysis of water. The more oxygen is present in the cell at the time of irradiation, the more it will intervene in the radical cascade by amplifying the cytotoxic effect. The presence of oxygen stabilizes free radicals causing DNA damage and reduces the tumor cell's ability to repair it, e.g. three-fold higher dose is required to kill some hypoxic cell lines. During fractionated radiotherapy, the situation becomes more complex because reoxygenation occurs between fractions, with some hypoxic cells reacquiring radiosensitivity [2]. Nevertheless, radiotherapy planning aims to deliver and certificate a homogeneous physical absorbed dose to the target volume, ignoring that oxygen distribution within the tumor microenvironment is not homogeneous, so the effective dose (in terms of DNA damage). Not surprisingly, clinical evidence points to the same direction with anemia identified as an adverse prognostic factor in cancer patients receiving radiotherapy. Hemoglobin levels in the patient (in the past), and low oxygen partial pressures in tumor tissues (nowadays) were also found to be predictive of local failure/poor prognosis after radiotherapy in hematological malignancies and many solid tumors [22, 10, 66, 63, 43, 19, 8, 40, 38, 27, 70]. This peculiar role of the oxygen effect prompted examining many approaches to circumventing hypoxia's therapeutic resistance. Alleviating hypoxia may delay cancer progression and improve response to oncological treatments. Hypoxia targeting methods are a very active area of preclinical and clinical research and include strategies to increase oxygen delivery or decrease tumor cells' consumption.

Our model has the ability to analyze the spatial distribution of the oxygen pressure deducing from different scenarios the importance of biological, mechanical and fluid dynamic parameters in the consequent hypoxia condition within the 3D vascularized tissue. Our results are in agreement with the mathematical model presented in [58]. Authors found that hypoxia (hypoxic fraction of tissue $p_{O_2} < 3\,mmHg$) can be abolished by reducing the consumption rate of 30%, while the same aim can be reached with an increase of factor 4 in flow rate, or still by a factor 11 in inlet p_{O_2}. Similarly, we found that, as a consequence of reducing the consumption rate of 50%, the volume fraction with $p_{O_2} < 5\,mmHg$ almost disappears, while a 2 fold variation in hematocrit induced a limited change in hypoxic volume. Thus, the results suggest that reducing oxygen consumption rate, e.g., by inhibiting the tumor mitochondrial respiration [14], may be more effective than improving oxygen content, interpreting the lack of agreement among clinical studies aiming to improve oxygen delivery. Alternative strategies have to be applied when hypoxia cannot be suppressed, or

oxygen consumption rate is too elevated. Optimal dose fractionation schemes, high linear energy transfer radiation (LET), not sensitive to oxygen distribution), and dose painting following hypoxia indications from diagnostic imaging are the most promising [11, 36].

4.2 Clinical applications for radiotherapy and limitations of an oxygen transfer model

A number of factors associated with the tumor microenvironment can contribute to the probability of local tumor control after fractionated RT. These factors have been summarized in the early phase of preclinical radiobiology by Withers as "the four Rs of Radiotherapy"[21]: recovery from sublethal damage, cell-cycle redistribution, cellular repopulation and tumor reoxygenation. Successively, Steel has suggested intrinsic cellular radiosensitivity as a fifth "R" to account for the different tolerance of tissues to fractionated irradiation [64]. Reasonably, when we refer to clinical studies, radiosensitivity could be considered as the only "R" of radiotherapy, including all other mentioned effects. The estimated radiobiological parameters (e.g. the α/β ratio [67]) are an average effect which mixes multiple tumor phenotypes (different cellular radiosensitivities, different repopulations and repair capabilities), treatment schedules (cell cycle phases) and patients' vasculature system (oxygen effect).

Among the four "Rs", oxygenation is currently the most promising to be addressed with clinical intervention and the unique strictly related to:

- *the tumor;* the chaotic level of the capillary network within the tumor mass can lead to a major state of tumor resistance. Clinical application in the field are favored by recent results with non-invasive imaging hypoxia detecting approaches that have allowed longitudinal evaluations on oxygen spatial and temporal changes throughout therapy. A computational model can be considered to help the interpretation of the measured oxygen distribution and to possibly design clinical strategies (e.g., dose painting [20]).

- *the patient;* we can quantify and differentiate among several levels of oxygenation even within the same type of tumor. The patient status can be modified by local or systemic approaches, improving tumor oxygenation and leading to better efficacy of the RT. A computational model can be applied to consider the effect of a systemic intervention that acts on blood pressure and oxygen concentration. A possible clinical aim could be identifying parameters that make reasonable and sufficient specific local or systemic intervention on the cardiovascular network or on the angiogenic factors.

- *the source of radiation;* if the previously describerd approaches could not be considered to improve the RT efficacy, we can act on the radiation type. Particularly, high-LET irradiation can be used to reduce the relevance of tumor hypoxia. The coupling of a biological model for considering the cell survival probability in a tumor tissue could be considered in a

computational model. A feasibility study to evaluate through a combined model the efficacy of photons, protons and carbon ions irradiation on a 3D tumor tissue irrorated at different capillary densities (thus different p_{O_2} concentrations) has been performed by our group [53].

The presented computational model can be considered as a tool for improving the understanding of radiotherapy resistance due to the oxygen concentration within the tumor tissue and its microenvironment. Neglecting the other abovementioned effects (i.e., recovery from sublethal damage, cell-cycle redistribution, cellular repopulation and cellular intrinsic radiosensitivity) is a limitation of the model. The explicit focus of this study is to show the possible role of oxygenation in tumor progression and response to therapies to improve the clinicians' awareness to the topic and favor the spread of an "oxygen metric" that should be considered along with the cancer staging and tumor volume when planning the radiotherapy treatment.

5 Conclusions

We conclude that the *oxygenation* of the vascular microenvironment is a multifactorial quantity, where each factor reacts differently to the chosen variation of the inputs. Among these factors, the oxygen consumption rate seems to be the one with the most substantial influence on the tissue's oxygenation. As addressed in the introduction, hypoxic cancer results in less sensitivity to both radiotherapy and chemotherapy. The effectiveness of such approaches has to be validated in clinical studies. However, many aspects could be profitably studied in-silico, using computational models that can consider the main features of realistic tumors (the geometry of the vasculature, p_{O_2} gradients, heterogeneity of p_{O_2}, oxygen consumption) and the processes of interest for radiotherapy (effects of fraction size, effects of different radiotherapy fractions, effects of LET) [11]. Computational modeling brings into the arena its peculiar ability to investigate the specific impact of factors that cannot be separated in the experimental setting.

The computational model presented here can be effectively used in this framework. It can quantitatively describe the microvascular oxygen transfer, taking into account effects at the tissue microenvironment and allowing for the description of spatial heterogeneity. Easy-to-tune boundary conditions and low computational burden make it suitable to describe different interest scenarios for radiotherapy, such as p_{O_2} levels in various histologies/risk classes, the effect of subsequent doses of radiotherapy, of different fraction size and radiation quality. The model already includes the possibility of mass transfer [3], which opens to its use in scenarios of combined oncological therapies involving both drugs and radiotherapy. Understanding the effect of radiotherapy on tumor vasculature functionality would be essential to maximize combined treatments' effectiveness.

Acknowledgments

This work is supported by the AIRC Investigator Grant IG21479 *Mechanistic computational modelling of radiation damage to microvasculature and of its effect on tumour microenvironment.*

References

[1] Alper, T., Howard-Flanders, P.: Role of oxygen in modifying the radiosensitivity of e. coli b. Nature **178**(4540), 978–979 (1956)

[2] Cao, X., Allu, S.R., Jiang, S., Jia, M., Gunn, J.R., Yao, C., LaRochelle, E.P., Shell, J.R., Bruza, P., Gladstone, D.J., et al.: Tissue po 2 distributions in xenograft tumors dynamically imaged by cherenkov-excited phosphorescence during fractionated radiation therapy. Nature communications **11**(1), 1–9 (2020)

[3] Cattaneo, L., Zunino, P.: A computational model of drug delivery through microcirculation to compare different tumor treatments. International Journal for Numerical Methods in Biomedical Engineering **30**(11), 1347–1371 (2014). https://doi.org/10.1002/cnm.2661

[4] Cattaneo, L., Zunino, P.: Computational models for fluid exchange between microcirculation and tissue interstitium. Networks and Heterogeneous Media **9**(1), 135–159 (2014)

[5] Celaya-Alcala, J.T., Lee, G.V., Smith, A.F., Li, B., Sakadžić, S., Boas, D.A., Secomb, T.W.: Simulation of oxygen transport and estimation of tissue perfusion in extensive microvascular networks: Application to cerebral cortex. Journal of Cerebral Blood Flow & Metabolism **41**(3), 656–669 (mar 2021). https://doi.org/10.1177/0271678X20927100

[6] D'Angelo, C., Quarteroni, A.: On the coupling of 1d and 3d diffusion-reaction equations. application to tissue perfusion problems. Mathematical Models and Methods in Applied Sciences **18**(8), 1481–1504 (2008)

[7] Dash, R., Bassingthwaighte, J.: Erratum: Blood hbo2 and hbco2 dissociation curves at varied o2, co2, ph, 2,3-dpg and temperature levels (annals of biomedical engineering (2004) 32:12 (1676-1693)). Annals of Biomedical Engineering **38**(4), 1683–1701 (2010). https://doi.org/10.1007/s10439-010-9948-y

[8] Dunphy, E.P., Petersen, I.A., Cox, R.S., Bagshaw, M.A.: The influence of initial hemoglobin and blood pressure levels on results of radiation therapy for carcinoma of the prostate. International Journal of Radiation Oncology* Biology* Physics **16**(5), 1173–1178 (1989)

[9] Endeward, V., Gros, G., Jürgens, K.D.: Significance of myoglobin as an oxygen store and oxygen transporter in the intermittently perfused human heart: a model study. Cardiovascular Research **87**(1), 22–29 (jul 2010). https://doi.org/10.1093/cvr/cvq036

[10] Evans, J., Bergsjfø, P.: The influence of anemia on the results of radiotherapy in carcinoma of the cervix. Radiology **84**(4), 709–717 (1965)

[11] Forster, J.C., Marcu, L.G., Bezak, E.: Approaches to combat hypoxia in cancer therapy and the potential for in silico models in their evaluation. Physica Medica **64**, 145–156 (2019)

[12] Fournié, M., Renon, N., Renard, Y., Ruiz, D.: Cfd parallel simulation using getfem++ and mumps. In: D'Ambra, P., Guarracino, M., Talia, D. (eds.) Euro-Par 2010 - Parallel Processing. pp. 77–88. Springer Berlin Heidelberg, Berlin, Heidelberg (2010)

[13] Gagnon, L., Smith, A.F., Boas, D.A., Devor, A., Secomb, T.W., Sakadžić, S.: Modeling of Cerebral Oxygen Transport Based on In vivo Microscopic Imaging of Microvascular Network Structure, Blood Flow, and Oxygenation. Frontiers in Computational Neuroscience **10**(August), 1–20 (2016). https://doi.org/10.3389/fncom.2016.00082

[14] Gallez, B., Neveu, M.A., Danhier, P., Jordan, B.: Manipulation of tumor oxygenation and radiosensitivity through modification of cell respiration. a critical review of approaches and imaging biomarkers for therapeutic guidance. Biochimica et Biophysica Acta - Bioenergetics **1858**(8), 700–711 (2017)

[15] Goldman, D.: Theoretical models of microvascular oxygen transport to tissue. Microcirculation **15**(8), 795–811 (2008). https://doi.org/10.1080/10739680801938289

[16] Goldman, D., Popel, A.: A computational study of the effect of capillary network anastomoses and tortuosity on oxygen transport. Journal of Theoretical Biology **206**(2), 181–194 (2000)

[17] Gould, I., Tsai, P., Kleinfeld, D., Linninger, A.: The capillary bed offers the largest hemodynamic resistance to the cortical blood supply. Journal of Cerebral Blood Flow and Metabolism **37**(1), 52–68 (2017)

[18] Gray, L.H., Conger, A., Ebert, M., Hornsey, S., Scott, O.: The concentration of oxygen dissolved in tissues at the time of irradiation as a factor in radiotherapy. The British journal of radiology **26**(312), 638–648 (1953)

[19] Greven, K.M., Solin, L.J., Hanks, G.E.: Prognostic factors in patients with bladder carcinoma treated with definitive irradiation. Cancer **65**(4), 908–912 (1990)

[20] Gérard, M., Corroyer-Dulmont, A., Lesueur, P., Collet, S., Chérel, M., Bourgeois, M., Stefan, D., Limkin, E., Perrio, C., Guillamo, J., Dubray, B., Bernaudin, M., Thariat, J., S., V.: Hypoxia Imaging and Adaptive Radiotherapy: A State-of-the-Art Approach in the Management of Glioma. Frontiers in Medicine **6**, 117 (Jun 2019). https://doi.org/10.3389/fonc.2019.01009

[21] H.R., W.: The Four R's of Radiotherapy. Advances in Radiation Biology **5**, 241–271 (1975), https://doi.org/10.1016/B978-0-12-035405-4.50012-8

[22] Hughes, V.S., Wiggins, J.M., Siemann, D.W.: Tumor oxygenation and cancer therapy—then and now. The British journal of radiology **92**(1093), 20170955 (2018)

[23] Intaglietta, M., Johnson, P., Winslow, R.: Microvascular and tissue oxygen distribution. Cardiovascular Research **32**(4), 632–643 (1996)

[24] Jain, R.K., Tong, R.T., Munn, L.L.: Effect of vascular normalization by antiangiogenic therapy on interstitial hypertension, peritumor edema, and lymphatic metastasis: Insights from a mathematical model. Cancer Research **67**(6), 2729–2735 (2007). https://doi.org/10.1158/0008-5472.CAN-06-4102

[25] Jarzyńska, M.: The application of practical kedem-katchalsky equations in membrane transport. Central European Journal of Physics **4**(4), 429–438 (2006). https://doi.org/10.2478/s11534-006-0034-x

[26] JR, L.: Capillary filtration-absorption balance reconsidered in light of dynamic extravascular factors. Experimental Physiology **76**(6), 825–857 (1991). https://doi.org/https://doi.org/10.1113/expphysiol.1991.sp003549

[27] Knocke, T.H., Weitmann, H.D., Feldmann, H.J., Selzer, E., Pötter, R.: Intratumoral po2-measurements as predictive assay in the treatment of carcinoma of the uterine cervix. Radiotherapy and Oncology **53**(2), 99–104 (1999)

[28] Köppl, T., Vidotto, E., Wohlmuth, B.: A 3D-1D coupled blood flow and oxygen transport model to generate microvascular networks. International Journal for Numerical Methods in Biomedical Engineering **36**(10) (oct 2020). https://doi.org/10.1002/cnm.3386

[29] Krogh, A.: The number and distribution of capillaries in muscles with calculations of the oxygen pressure head necessary for supplying the tissue. The Journal of Physiology **52**(6), 409–415 (1919). https://doi.org/10.1113/jphysiol.1919.sp001839

[30] Laurino, F., Coclite, A., Tiozzo, A., Decuzzi, P., Zunino, P.: A hierarchical multiscale model for predicting the vascular behavior of blood-borne nanomedicines. International Journal for

Multiscale Computational Engineering **18**(3), 335–359 (2020). https://doi.org/10.1615/IntJMultCompEng.2020033358

[31] Laurino, F., Zunino, P.: Derivation and analysis of coupled pdes on manifolds with high dimensionality gap arising from topological model reduction. ESAIM: Mathematical Modelling and Numerical Analysis **53**(6), 2047–2080 (2019)

[32] Linninger, A., Hartung, G., Badr, S., Morley, R.: Mathematical synthesis of the cortical circulation for the whole mouse brain-part i. theory and image integration. Computers in Biology and Medicine **110**, 265–275 (2019)

[33] Lücker, A., Secomb, T.W., Weber, B., Jenny, P.: The relative influence of hematocrit and red blood cell velocity on oxygen transport from capillaries to tissue. Microcirculation **24**(3), e12337 (apr 2017). https://doi.org/10.1111/micc.12337

[34] Lücker, A., Weber, B., Jenny, P.: A dynamic model of oxygen transport from capillaries to tissue with moving red blood cells. American Journal of Physiology - Heart and Circulatory Physiology **308**(3), H206–H216 (2015). https://doi.org/10.1152/ajpheart.00447.2014

[35] Macedo-Silva, C., Miranda-Gonçalves, V., Henrique, R., Jerónimo, C., Bravo, I.: The critical role of hypoxic microenvironment and epigenetic deregulation in esophageal cancer radioresistance. Genes **10**(11), 927 (2019)

[36] Martin, J.D., Fukumura, D., Duda, D.G., Boucher, Y., Jain, R.K.: Reengineering the tumor microenvironment to alleviate hypoxia and overcome cancer heterogeneity. Cold Spring Harbor perspectives in medicine **6**(12), a027094 (2016)

[37] Michaelis, L., Menten, M.L., Johnson, K.A., Goody, R.S.: The original michaelis constant: translation of the 1913 michaelis-menten paper. Biochemistry **50**(39), 8264—8269 (October 2011). https://doi.org/10.1021/bi201284u

[38] Movsas, B., Chapman, J.D., Hanlon, A.L., Horwitz, E.M., Greenberg, R.E., Stobbe, C., Hanks, G.E., Pollack, A.: Hypoxic prostate/muscle po2 ratio predicts for biochemical failure in patients with prostate cancer: preliminary findings. Urology **60**(4), 634–639 (2002)

[39] Munoz, C.J., Lucas, A., Williams, A.T., Cabrales, P.: A Review on Microvascular Hemodynamics. Critical Care Clinics **36**(2), 293–305 (apr 2020). https://doi.org/10.1016/j.ccc.2019.12.011

[40] Nordsmark, M., Bentzen, S.M., Rudat, V., Brizel, D., Lartigau, E., Stadler, P., Becker, A., Adam, M., Molls, M., Dunst, J., et al.: Prognostic value of tumor oxygenation in 397 head and neck tumors after primary radiation

therapy. an international multi-center study. Radiotherapy and oncology **77**(1), 18–24 (2005)

[41] Obrist, D., Weber, B., Buck, A., Jenny, P.: Red blood cell distribution in simplified capillary networks. Philosophical Transactions of the Royal Society A: Mathematical, Physical and Engineering Sciences **368**(1921), 2897–2918 (2010)

[42] Offeddu, G., Possenti, L., Loessberg-Zahl, J., Zunino, P., Roberts, J., Han, X., Hickman, D., Knutson, C., Kamm, R.: Application of transmural flow across in vitro microvasculature enables direct sampling of interstitial therapeutic molecule distribution. Small **15**(46) (2019). https://doi.org/10.1002/smll.201902393

[43] Overgaard, J., Hansen, H.S., Overgaard, M., Bastholt, L., Berthelsen, A., Specht, L., Lindeløv, B., Jørgensen, K.: A randomized double-blind phase iii study of nimorazole as a hypoxic radiosensitizer of primary radiotherapy in supraglottic larynx and pharynx carcinoma. results of the danish head and neck cancer study (dahanca) protocol 5-85. Radiotherapy and Oncology **46**(2), 135–146 (1998)

[44] Pittman, R.N.: Oxygen Transport in the Microcirculation and Its Regulation. Microcirculation **20**(2), 117–137 (feb 2013). https://doi.org/10.1111/micc.12017

[45] Popel, A.S.: Theory of oxygen transport to tissue. Critical Reviews in Biomedical Engineering **17**(3), 257–321 (1989)

[46] Popel, A., Johnson, P.: Microcirculation and hemorheology. Annual Review of Fluid Mechanics **37**, 43–69 (2005). https://doi.org/10.1146/annurev.fluid.37.042604.133933

[47] Possenti, L., Casagrande, G., Di Gregorio, S., Zunino, P., Costantino, M.: Numerical simulations of the microvascular fluid balance with a nonlinear model of the lymphatic system. Microvascular Research **122**, 101–110 (2019). https://doi.org/10.1016/j.mvr.2018.11.003

[48] Possenti, L., Di Gregorio, S., Casagrande, G., Costantino, M., Rancati, T., Zunino, P.: A global sensitivity analysis approach applied to a multiscale model of microvascular flow. Computer Methods in Biomechanics and Biomedical Engineering pp. 1–10 (2020)

[49] Possenti, L., di Gregorio, S., Gerosa, F., Raimondi, G., Casagrande, G., Costantino, M., Zunino, P.: A computational model for microcirculation including fahraeus-lindqvist effect, plasma skimming and fluid exchange with the tissue interstitium. International Journal for Numerical Methods in Biomedical Engineering **35**(3) (2019). https://doi.org/10.1002/cnm.3165

[50] Pries, A.R., Secomb, T.W.: Microvascular blood viscosity in vivo and the endothelial surface layer. American journal of physiology. Heart and circulatory physiology **289**(6), H2657–H2664 (2005). https://doi.org/10.1152/ajpheart.00297.2005

[51] Pries, A.R., Secomb, T.W., Gessner, T., Sperandio, M.B., Gross, J.F., Gaehtgens, P.: Resistance to blood flow in microvessels in vivo. Circulation Research **75**(5), 904–915 (nov 1994). https://doi.org/10.1161/01.RES.75.5.904

[52] Rasmussen, P.M., Secomb, T.W., Pries, A.R.: Modeling the hematocrit distribution in microcirculatory networks: A quantitative evaluation of a phase separation model. Microcirculation **25**(3), 1–17 (2018). https://doi.org/10.1111/micc.12445

[53] Rosati, R., Possenti, L., Cicchetti, A., Costantino, M., Rancati, T., Zunino, P.: A multiscale model for oxygen delivery and radiation damage within the microenvironment. EFOMP - 3rd European Congress of Medical Physics (16-19 Jun 2021)

[54] Sakadžić, S., Roussakis, E., Yaseen, M., Mandeville, E., Srinivasan, V., Arai, K., Ruvinskaya, S., Devor, A., Lo, E., Vinogradov, S., Boas, D.: Two-photon high-resolution measurement of partial pressure of oxygen in cerebral vasculature and tissue. Nature Methods **7**(9), 755–759 (2010). https://doi.org/10.1038/nmeth.1490

[55] Scott, O.: Some aspects of the effect of ionizing radiation on tumors in experimental animals. In: Advances in biological and medical physics, vol. 6, pp. 121–173. Elsevier (1959)

[56] Secomb, T.W.: Blood flow in the microcircaulation. Annual Review of Fluid Mechanics **49**, 443–461 (2017). https://doi.org/10.1146/annurev-fluid-010816-060302

[57] SECOMB, T., HSU, R., BEAMER, N., COULL, B.: Theoretical simulation of oxygen transport to brain by networks of microvessels: Effects of oxygen supply and demand on tissue hypoxia. Microcirculation **7**(4), 237–247 (2000). https://doi.org/doi.org/10.1111/j.1549-8719.2000.tb00124.x

[58] Secomb, T., Hsu, R., Ong, E., Gross, J., Dewhirst, M.: Analysis of the effects of oxygen supply and demand on hypoxic fraction in tumors. Acta Oncologica **34**(3), 313–316 (1995)

[59] Secomb, T., Hsu, R., Park, E., Dewhirst, M.: Green's function methods for analysis of oxygen delivery to tissue by microvascular networks. Annals of Biomedical Engineering **32**(11), 1519–1529 (2004)

[60] Secomb, T., Pries, A.: The microcirculation: Physiology at the mesoscale. Journal of Physiology **589**(5), 1047–1052 (2011)

[61] Sefidgar, M., Soltani, M., Raahemifar, K., Sadeghi, M., Bazmara, H., Bazargan, M., Mousavi Naeenian, M.: Numerical modeling of drug delivery in a dynamic solid tumor microvasculature. Microvascular Research **99**, 43–56 (2015). https://doi.org/10.1016/j.mvr.2015.02.007

[62] Sové, R.J., Goldman, D., Fraser, G.M.: A computational model of the effect of capillary density variability on oxygen transport, glucose uptake, and insulin sensitivity in prediabetes. Microcirculation **24**(2), e12342 (feb 2017). https://doi.org/10.1111/micc.12342

[63] Stadler, P., Becker, A., Feldmann, H.J., Hänsgen, G., Dunst, J., Würschmidt, F., Molls, M.: Influence of the hypoxic subvolume on the survival of patients with head and neck cancer. International Journal of Radiation Oncology* Biology* Physics **44**(4), 749–754 (1999)

[64] Steel, G., McMillan, T., Peacock, J.: The 5Rs of Radiobiology. International Journal of Radiation Biology **56**(6), 1045–1048 (2009). https://doi.org/10.1080/09553008914552491

[65] Sweeney, P., D'esposito, A., Walker-Samuel, S., Shipley, R.: Modelling the transport of fluid through heterogeneous, whole tumours in silico. PLoS Computational Biology **15**(6) (2019)

[66] Takeshi, K., Katsuyuki, K., Yoshiaki, T., Tadayoshi, M., Akira, M., Katsumi, M.: Definitive radiotherapy combined with high-dose-rate brachytherapy for stage iii carcinoma of the uterine cervix: retrospective analysis of prognostic factors concerning patient characteristics and treatment parameters. International Journal of Radiation Oncology* Biology* Physics **41**(2), 319–327 (1998)

[67] Thames, H., Withers, H., Peters, L., Fletcher, G.: Changes in early and late radiation responses with altered dose fractionation: implications for dose-survival relationships. International Journal of Radiation Oncology Biology and Physics **8**(2), 219–226 (Feb 1982). https://doi.org/10.1016/0360-3016(82)90517-x

[68] Tsai, A., Johnson, P., Intaglietta, M.: Oxygen gradients in the microcirculation. Physiological Reviews **83**(3), 933–963 (2003)

[69] Vaupel, P., Kallinowski, F., Okunieff, P.: Blood flow, oxygen and nutrient supply, and metabolic microenvironment of human tumors: a review. Cancer research **49**(23), 6449–6465 (1989)

[70] Walsh, J.C., Lebedev, A., Aten, E., Madsen, K., Marciano, L., Kolb, H.C.: The clinical importance of assessing tumor hypoxia: relationship of tumor hypoxia to prognosis and therapeutic opportunities. Antioxidants & redox signaling **21**(10), 1516–1554 (2014)

[71] Wang, Z., Zhao, Q., Cui, M., Pang, S., Wang, J., Liu, Y., Xie, L.: Probing temperature- and ph-dependent binding between quantum dots and bovine serum albumin by fluorescence correlation spectroscopy. Nanomaterials **7**(5) (2017). https://doi.org/10.3390/nano7050093

[72] Welter, M., Fredrich, T., Rinneberg, H., Rieger, H.: Computational model for tumor oxygenation applied to clinical data on breast tumor hemoglobin concentrations suggests vascular dilatation and compression. PLoS ONE **11**(8) (2016). https://doi.org/10.1371/journal.pone.0161267

[73] Zhang, C., Bélanger, S., Pouliot, P., Lesage, F.: Measurement of local partial pressure of oxygen in the brain tissue under normoxia and epilepsy with phosphorescence lifetime microscopy. PLoS ONE **10**(8) (2015). https://doi.org/10.1371/journal.pone.0135536

Supplementary materials of: A mesoscale computational model for microvascular oxygen transfer

Luca Possenti[1,2,*], Alessandro Cicchetti[2,*], Riccardo Rosati[1], Daniele Cerroni[3], Maria Laura Costantino[1], Tiziana Rancati[2], Paolo Zunino[3]

[1] Department of Chemistry, Materials and Chemical Engineering "Giulio Natta", Politecnico di Milano
[2] Prostate Cancer Program, Fondazione IRCCS Istituto Nazionale dei Tumori di Milan
[3] MOX, Department of Mathematics, Politecnico di Milano

6 Numerical discretization and solvers

6.1 Treatment of non-linear terms

The 3D-1D oxygen transport model consists of a non-linear system of partial differential equations. The model presents two relevant non-linear terms: the Michaelis-Menten formula and the oxyhemoglobin concentration as function of the saturation of RBCs. In the presence of non-linear terms, iterative methods are used to solve the problem. In practice, the solution at iteration k is computed as a correction of the solution at the previous iteration $k-1$, until an error metric is small enough to be less than a given threshold. Here, we apply a fixed point method to linearize the system of equations by evaluating the reaction term in the tissue and the oxyhemoglobin concentration in the micro-vessels at the previous iteration. More precisely, we define the new coefficient, $\Psi^{(k-1)}$ as the oxyhemoglobin concentration at the previous iteration:

$$\Psi^{(k-1)} = k_1 \; H \; \frac{\left(C_v^{(k-1)}\right)^{\gamma-1}}{\left(C_v^{(k-1)}\right)^{\gamma} + k_2} \tag{23}$$

Such formulation of the oxyhemoglobin term highlights the effect of the transport of free oxygen with respect to the bound-hemoglobin oxygen. Then, the blood velocity can be re-written as follows:

$$u_v^{(k-1)} = u_v \; (1 + \Psi^{(k-1)}); \tag{24}$$

Using (23) and (24), the linearized model is:

$$\begin{cases} \nabla \cdot \left(-D_t \nabla C_t^{(k)} + \mathbf{u}_t \; C_t^{(k)} \right) + V_{max} \; \dfrac{C_t^{(k)}}{C_t^{(k-1)} + \alpha_t \; p^{m_{50}}} \\ = \left[2\pi R \; P_{O_2} (C_v^{(k)} - \overline{C}_t^{(k)}) + (1 - \sigma_{O_2}) \; \left(\frac{C_v^{(k)} + \overline{C}_t^{(k)}}{2} \right) \; \phi_v \right] \delta_\Lambda \quad \text{on } \Omega \,, \\ \pi R^2 \dfrac{\partial}{\partial s} \left(-D_v \dfrac{\partial C_v^{(k)}}{\partial s} + u_v^{(k-1)} \; C_v^{(k)} \right) \\ = -2\pi R \; P_{O_2} (C_v^{(k)} - \overline{C}_t^{(k)}) + (1 - \sigma_{O_2}) \; \left(\frac{C_v^{(k)} + \overline{C}_t^{(k)}}{2} \right) \; \phi_v \quad \text{on } \Lambda \,, \end{cases} \tag{25}$$

complemented with the same initial and boundary conditions of (13).

6.2 Numerical approximation

The discretization of problem is achieved by means of the finite element method. One of the main advantages of our formulation is that the partitions of Ω and Λ are completely independent. For this reason we address the two approximations separately. We denote with $\mathcal{T}$ an admissible family of partitions of Ω into tetrahedrons K, namely $\Omega = \bigcup_{K \in \mathcal{T}_t^h} K$, that satisfies the usual conditions of a conforming triangulation of Ω. Here, h denotes the mesh characteristic size, i.e. $h = \max_{K \in \mathcal{T}_t^h} k_K$, being h_K the diameter of K. Moreover, we are implicitly assuming that Ω is a *polygonal* domain. The solutions of the weak problem are approximated using continuous piecewise-polynomial finite elements for the concentration, in particular we have $Y_k^h := \{ f_h \in C^0(\Omega), \; f_h|_K \in P_k(K) \quad \forall K \in \mathcal{T}_t^h \}$, for every integer $k \geq 0$, where P_k indicates the standard space of polynomials of degree $\leq k$ in the variables $\mathbf{x} = (x_1, \ldots, x_d)$.

Concerning the capillary network, we discretize the network branches as separate sub-domains. Each branch Λ_i is approximated by a piecewise linear 1D line, denoted with Λ_i^h. More precisely the Λ_i^h is a partition of the i-th network branch made by a sufficiently large number of segments, named $S \subset \Lambda_i^h$. The solution of (22) over a given branch Λ_i^h is approximated using continuous piecewise-polynomial finite element spaces, precisely $X_k^h(\Lambda) := \{ g_h \in C^0(\Lambda), \, g_h|_S \in P_k(S) \quad \forall S \in \Lambda^h \}$, for every integer $k \geq 0$. The discrete formulation arising from (22) is easily obtained by projecting the equations on the discrete spaces $Q_t^h = Y_k^h(\Omega)$ and $Q_v^h = X_k^h(\Lambda)$ for k ≥ 0.

6.3 Algebraic formulation

In order to calculate the numerical solution of the problem, let us introduce the algebraic formulation of the complete problem. It is worth nothing that the problem has been linearized, so the resulting linear system has to be solved at each step of the fix-point method previously addressed.

The number of degrees of freedom (DOFs) of the discrete spaces Q_t^h and Q_v^h is $N_t^h = dim(Q_t^h)$ and $N_v^h = dim(Q_v^h)$ and the finite elements basis function,

φ are $\{\varphi_t^i\}_{i=1}^{N_t^h}$ for Q_t^h and $\{\varphi_v^j\}_{j=1}^{N_v^h}$ for Q_v^h. Then, the numerical solution for the oxygen concentration can be written as a linear combination of those basis functions $C_t^h(\mathbf{x}) = \sum_{i=1}^{N_t^h} {c_t}^{h,i(k)}\ \varphi_t^i(\mathbf{x}),\ \ \forall \mathbf{x} \in Q_t^h\ C_v^h(s) = \sum_{j=1}^{N_v^h} {c_v}^{h,j(k)}\ \varphi_v^j(s)$. Substituting these expressions in the weak discrete problem and exploiting the linearity of the inner product, we obtain the following linear system for each iterative step:

$$\begin{bmatrix} \mathbb{D}_t + \mathbb{A}_t + \mathbb{R}_t + \mathbb{B}_{tt} & \mathbb{B}_{tv} \\ \mathbb{B}_{vt} & \mathbb{D}_v + \mathbb{A}_v + \mathbb{B}_{vv} \end{bmatrix} \begin{bmatrix} \mathbf{C}_t^{h^{(k)}} \\ \mathbf{C}_v^{h^{(k)}} \end{bmatrix} = \begin{bmatrix} \mathbb{F}_t \\ \mathbb{F}_v \end{bmatrix}. \qquad (26)$$

The submatrices and subvectors in (26) are defined as follows:

$$[\mathbb{D}_t]_{ij} := (D_t^*\ \boldsymbol{\varphi}_t^j, \boldsymbol{\varphi}_t^i)_\Omega + (\beta_t \boldsymbol{\varphi}_t^j, \boldsymbol{\varphi}_t^i)_{\partial\Omega_{MIX}}, \qquad \mathbb{D}_t \in \mathbb{R}^{N_t^h \times N_t^h},$$

$$[\mathbb{A}_t]_{ij} := (\boldsymbol{u_t}^h \cdot \nabla \boldsymbol{\varphi}_t^j, \boldsymbol{\varphi}_t^i)_\Omega + (\nabla \cdot \boldsymbol{u_t}^h\ \boldsymbol{\varphi}_t^j, \boldsymbol{\varphi}_t^i)_\Omega, \qquad \mathbb{A}_t \in \mathbb{R}^{N_t^h \times N_t^h},$$

$$[\mathbb{R}_t]_{ij} := (\frac{M_0}{C_t^{h,(k-1)} + K_M}\ \boldsymbol{\varphi}_t^j, \boldsymbol{\varphi}_t^i)_\Omega, \qquad \mathbb{R}_t \in \mathbb{R}^{N_t^h \times N_t^h},$$

$$[\mathbb{D}_v]_{ij} := (\pi R^{*2} D_v^*\ \frac{\partial \boldsymbol{\varphi}_v^j}{\partial s}, \frac{\partial \boldsymbol{\varphi}_v^i}{\partial s})_\Omega, \qquad \mathbb{D}_v \in \mathbb{R}^{N_v^h \times N_v^h},$$

$$[\mathbb{A}_v]_{ij} := (\pi R^{*2}\ u_v^{*h,(k-1)} \frac{\partial \boldsymbol{\varphi}_v^j}{\partial s}, \boldsymbol{\varphi}_v^i)_\Omega + (\pi R^{*2}\ \frac{\partial u_v^{*h,(k-1)}}{\partial s} \boldsymbol{\varphi}_v^j, \boldsymbol{\varphi}_v^i)_\Omega + \quad \mathbb{A}_v \in \mathbb{R}^{N_v^h \times N_v^h},$$
$$+ (\pi R^{*2}\ \beta_v \boldsymbol{\varphi}_v^j, \boldsymbol{\varphi}_v^i)_{\partial\Lambda_{OUT}},$$

$$[\mathbb{B}_{tt}]_{ij} := -(2\pi R^* [P_l^* + \frac{L_p^*}{2}(1-\sigma_{oxy})\ P\ (P_v - P_t - \sigma\Delta\pi)] \boldsymbol{\varphi}_t^j, \boldsymbol{\varphi}_t^i)_\Omega, \quad \mathbb{B}_{tt} \in \mathbb{R}^{N_t^h \times N_t^h},$$

$$[\mathbb{B}_{tv}]_{ij} := +(2\pi R^* [P_l^* + \frac{L_p^*}{2}(1-\sigma_{oxy})\ P\ (P_v - P_t - \sigma\Delta\pi)] \boldsymbol{\varphi}_t^j, \boldsymbol{\varphi}_v^i)_\Omega, \quad \mathbb{B}_{tv} \in \mathbb{R}^{N_t^h \times N_v^h},$$

$$[\mathbb{B}_{vv}]_{ij} := -(2\pi R^* [P_l^* + \frac{L_p^*}{2}(1-\sigma_{oxy})\ P\ (P_v - P_t - \sigma\Delta\pi)] \boldsymbol{\varphi}_v^j, \boldsymbol{\varphi}_v^i)_\Omega, \quad \mathbb{B}_{vv} \in \mathbb{R}^{N_v^h \times N_v^h},$$

$$[\mathbb{B}_{vt}]_{ij} := +(2\pi R^* [P_l^* + \frac{L_p^*}{2}(1-\sigma_{oxy})\ P\ (P_v - P_t - \sigma\Delta\pi)] \boldsymbol{\varphi}_v^j, \boldsymbol{\varphi}_t^i)_\Omega, \quad \mathbb{B}_{vt} \in \mathbb{R}^{N_v^h \times N_t^h},$$

$$[\mathbb{F}_t]_i := -(\beta_t \; c_{0,t} \; \boldsymbol{\varphi}_t^i)_{\partial\Omega_{MIX}}, \qquad \mathbb{F}_t \in \mathbb{R}^{N_t^h},$$

$$[\mathbb{F}_v]_i := -(\pi {R^*}^2 \; \beta_v \; c_{0,v} \; \boldsymbol{\varphi}_v^i)_{\partial\Lambda_{OUT}}, \qquad \mathbb{F}_v \in \mathbb{R}^{N_v^h},$$

Where u_v^* is:

$$u_v^{*(k-1)} = u_v \; (1 + k_1 \; H \; \frac{C_v^{(k-1)^{\gamma-1}}}{C_v^{(k-1)^{\gamma}} + k_2})$$

7 Additional results on bifurcations and anastomoses

For the purpose of validation, in particular for the behavior of the model in proximity of bifurcations and anastomoses, we present here the following results. The geometrical model consists of a Y-shaped configuration, where all branches have the same length. The radii of the daughter branches are calculated on the basis of the Murray's law: $R_{in_0}^3 \simeq R_{out_1}^3 + R_{out_2}^3$, where index (0) denotes the parent vessel and (1), (2) are the daughter channels for the bifurcation case, while for the anastomosis the flow direction is reversed. In particular, the radii are $R_{in_0} = 6 \; \mu m$, $R_{in_1} = 4 \; \mu m$ and $R_{out_2} = 5 \; \mu m$.

The characteristic parameters have been set according to [49], and Table 1. As boundary conditions for the fluid dynamics problem and hematocrit transport, we set an inlet pressure of 32 $mmHg$ and an inlet hematocrit value at 0.45, then, at the outlet we set an outlet pressure of 28.5 $mmHg$. We set a Neumann condition for all the tissue faces and the outlet of the vessel, instead, we imposed a Dirichlet condition set to $C_{v_{in}}$ at the inlet.

For what concerns the oxygen transport simulations, the results are reported in Figure 7. We see that the free oxygen concentration is a continuous quantity at the junction. As discussed before, this property indirectly enforces the mass balance constraint. The free oxygen concentration varies between the daughter branches according to the 10% variation of the radius. For example, taking into account the lower branch, the oxygen tends to diffuse more easily due to a decreasing in velocity. It is interesting to analyze also the the variation along the branches of oxyhemoglobin, C_{HbO_2}, which jumps from one branch to another, due to the linear dependence of the hematocrit, which is also discontinuous at junctions.

For the anastomosis simulation, the flow is reversed by switching the inlet and outlet conditions and maintaining the same pressure drop as for the bifurcation. Precisely, we set $C_{v_{in}}$ as Dirichlet conditions at the two inlets of the vessels and Neumann condition at the single outlet of the anastomosis; we imposed a Neumann condition for all faces of the tissue domains. We simulate a particular case where the hematocrit is set at different values at the inlet of the anastomosis, namely, $H_0 = 0.35$ (*lower branch*) and $H_1 = 0.45$ (*upper branch*).

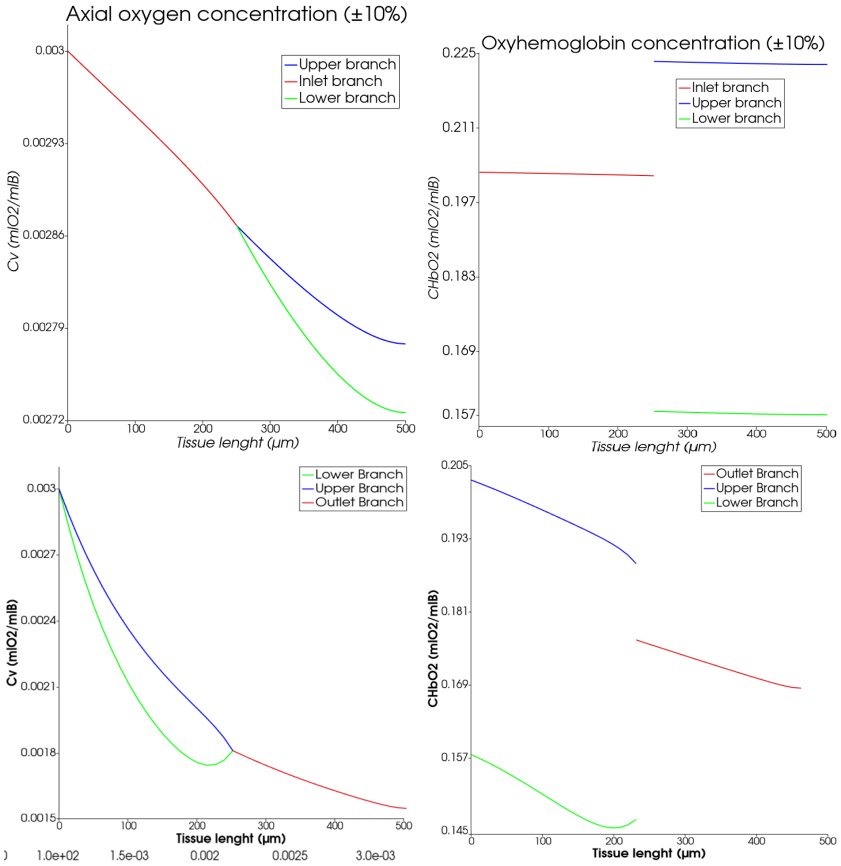

Figure 7: Oxygen concentration along the parent and daughter branches. The *red* curve is the concentration in bifurcation inlet, the *blue* curve is the upper branch and the *green* curve is the lower branch. On the top left panel we show the free concentration C_v and on the top right panel we report the oxyhemoglobin, C_{HbO_2}. The corresponding results for the anastomosis are reported on the bottom panel.

As shown in figure 7 (bottom panel), the free oxygen concentration has a non-monotone trend in the lower branch. This fact can be interpreted observing that the fluid moves with different velocity in the two branches, and so the Péclet number changes. More precisely, the lower branch has a lower Péclet number, due to the lower flow rate. For this reason, C_v features a higher gradient along the vessel axis, but however the continuity of the concentration profile must be restored at the junction, giving rise to a slight increase of the concentration value with respect to the inner part of the lower branch. The oxyhemoglobin concentration has a similar trend than for the bifurcation, although it is slightly affected by the variation of C_v.

MOX Technical Reports, last issues

Dipartimento di Matematica
Politecnico di Milano, Via Bonardi 9 - 20133 Milano (Italy)

84/2021 Torti, A.; Galvani, M.; Urbano, V.; Arena, M.; Azzone, G.; Secchi, P.; Vantini, S.
Analysing transportation system reliability: the case study of the metro system of Milan

85/2021 Cavinato, L., Gozzi, N., Sollini, M., Carlo-Stella, C., Chiti, A., & Ieva, F.
Recurrence-specific supervised graph clustering for subtyping Hodgkin Lymphoma radiomic phenotypes

83/2021 Colasuonno, F.; Ferrari F.; Gervasio, P.; Quarteroni, A.
Some evaluations of the fractional p-Laplace operator on radial functions

80/2021 Sollini, M., Bartoli, F., Cavinato, L., Ieva, F., Ragni, A., Marciano, A., Zanca, R., Galli, L., Pai
[18F]FMCH PET/CT biomarkers and similarity analysis to refine the definition of oligometastatic prostate cancer

81/2021 Massi, M.C.; Gasperoni, F.; Ieva, F.; Paganoni, A.
Feature Selection for Imbalanced Data with Deep Sparse Autoencoders Ensemble

79/2021 Ferraccioli, F.; Sangalli, L.M.; Finos, L.
Some first inferential tools for spatial regression with differential regularization

82/2021 Massi, M.C.; Ieva, F.
Learning Signal Representations for EEG Cross-Subject Channel Selection and Trial Classification

78/2021 Bucelli, M.; Dede', L.; Quarteroni, A.; Vergara, C.
Partitioned and monolithic algorithms for the numerical solution of cardiac fluid-structure interaction

75/2021 Cicci, L.; Fresca, S.; Pagani, S.; Manzoni, A.; Quarteroni, A.
Projection-based reduced order models for parameterized nonlinear time-dependent problems arising in cardiac mechanics

73/2021 Marcinno, F.; Zingaro, A.; Fumagalli, I.; Dede', L.; Vergara, C.
A computational study of blood flow dynamics in the pulmonary arteries